Air Force Institute of Technology

AFIT Scholar

Cesium Absorption Spectrum Perturbed by Argon: Observation of Non-Lorentzian Far Wings

Gordon E. Lott

CESIUM ABSORPTION SPECTRUM PERTURBED BY ARGON:

OBSERVATION OF NON-LORENTZIAN WING PROPERTIES

THESIS

Gordon E. Lott, Second Lieutenant, USAF

AFIT/APPLPHY/ENP/12-M08

DEPARTMENT OF THE AIR FORCE
AIR UNIVERSITY

AIR FORCE INSTITUTE OF TECHNOLOGY

Wright-Patterson Air Force Base, Ohio

The views expressed in this document are those of the author and do not reflect the official policy or position of the United States Air Force, the United States Department of Defense or the United States Government. This material is declared a work of the U.S. Government and is not subject to copyright protection in the United States.

AFIT/APPLPHY/ENP/12-M08

CESIUM ABSORPTION SPECTRUM PERTURBED BY ARGON:

OBSERVATION OF NON-LORENTZIAN WING PROPERTIES

THESIS

Presented to the Faculty

Department of Engineering Physics

Graduate School of Engineering and Management

Air Force Institute of Technology

Air University

Air Education and Training Command

in Partial Fulfillment of the Requirements for the

Degree of Master of Science in Applied Physics

Gordon E. Lott, BS

Second Lieutenant, USAF

March 2012

DISTRIBUTION STATEMENT A.
APPROVED FOR PUBLIC RELEASE; DISTRIBUTION UNLIMITED.

CESIUM ABSORPTION SPECTRUM PERTURBED BY ARGON:

OBSERVATION OF NON-LORENTZIAN WING PROPERTIES

Gordon E. Lott, BS
Second Lieutenant, USAF

Approved:

_____   *5 March 2012*

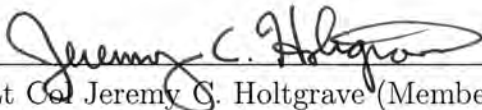Glen P. Perram, PhD (Chairman)   Date

_____   *5 March 2012*

David E. Weeks, PhD (Member)   Date

_____   *5 March 2012*

Lt Col Jeremy C. Holtgrave (Member)   Date

Abstract

A 1.33 m scanning monochromator with a PMT detector was used to observe the absorption spectra, and far wings, of the D_1 and D_2 lines of cesium (Cs) perturbed by argon (Ar). A heat pipe was used to control the Cs concentration and Ar pressure and allow for a broad range of spectra to be collected. Spectra were collected at heat pipe temperatures of 50, 75, 100, 125, 150, and 175 °C, corresponding to Cs concentrations of approximately 6×10^{11}, 4×10^{12}, 2×10^{13}, 5×10^{13}, 2×10^{14}, and 9×10^{14} cm^{-3}. These spectra were collected at each Ar buffer gas pressure of 484, 746, 1124, 1504, 1884, and 2280 Torr. The spectra were collected for wavelengths from 8250 Å to 9100 Å. The blue satellite of the D_2 absorption line was measured to be at a wavelength of $\approx 8367 \pm 0.8$ Å for Ar pressures from 500 Torr to 2280 Torr. A linear relationship between the D_2 wing cross section and increasing Ar pressure was observed for pressures from 100 Torr to 1504 Torr. The quantum quasi static approach as well as the static limit of Anderson-Talman theory was used to predict the far wing line-shape of the D_1 and D_2 lines from Cs-Ar interaction potential energy curves calculated by L. Blank [1], and were compared to measured spectra.

Acknowledgements

v

Table of Contents

List of Figures

x

List of Tables

CESIUM ABSORPTION SPECTRUM PERTURBED BY ARGON: OBSERVATION OF NON-LORENTZIAN WING PROPERTIES

I. Introduction

High Energy Lasers for Military Applications

The laser was first created in 1960 by Ted Maiman and has recently celebrated its 50th anniversary [2, p. 5]. Since then, the laser has come to be used commercially and privately throughout the world. The idea of a laser still usually conjures up some idea of a powerful destructive beam despite its common usage. This is perhaps partly because we all know that simply using a magnifying glass to focus sunlight things can be burnt and destroyed. Light can be a powerful weapon. The ability to engage a target at the speed of light and destroy it in seconds is a powerful proposition, and in 1963, three years after their invention, the Department of Defense (DoD) began researching the possible uses of this technology [2, p. 7].

Several systems have been developed within the DoD to take advantage of laser technology, the Air Born Laser (ABL), and the Advanced Tactical Laser (ATL). These systems have demonstrated the capabilities mentioned in addition to others [3, 4]. These weapons allow for extreme precision and speed of engagement, and have both strategic and tactical applications. It is true that traditional forms of weaponry are very good at their designed job. If a person, vehicle, or building (typical military targets) needs to be destroyed, a bomb or a bullet will work just fine. The utility of the laser becomes most apparent when looking at the defensive side of operations. President Reagan spurred one such use with his "Star Wars" defense budget and

1

began new defense programs. The express purpose of these programs was coming up with an alternative to the Mutually Assured Destruction (MAD) defensive posture the USA had with the Soviet Union at the time. The idea was to develop a way to defend against a missile attack by destroying the missile before it could deliver its payload. Ten years later, during the Gulf War, one of the major threats to American soldiers' lives were the ballistic missiles used by Saddam Hussein. The only way, even then, to effectively defend against such an attack was to find the missiles before they were launched. A way to destroy the missile while it was in flight to its target would have been an extremely powerful defensive weapon in both contexts.

Patriot missiles were able to provide some defense during the Gulf War, but had problems such as the missile debris falling on friendly territory and extremely precise tracking and path prediction requirements [2, p. 19]. A missile needing to travel 2 miles to a target missile would need to know the location of the missile 3.6 seconds later, if it is traveling at 2000 mph, which means the target, if it moves at half the speed, will have traveled a mile. A High Energy Laser (HEL) engages the target at the speed of light, 187281 miles a second. Using the same scenario the light would reach the target 108 milliseconds after being fired, the target would have moved 4 tenths of an inch, essentially point and shoot, tracking the target for 1 second over the course of 0.6 miles. An air or space based laser could do this before the missile reached friendly territory. The same idea can be applied to mortars or hand launched rockets on a more tactical level.

Three of the important aspects of a weapons class laser are the power output, the beam quality, and the magazine depth. Powers are needed from kilowatts to megawatts with beam qualities of $M^2 \approx 1$. Both of these have been demonstrated in the past, such as with Chemical Oxygen Iodine Lasers (COILs) which were used in the ABL. The limiting factors of chemical lasers is their magazine depth due to

2

burning up the chemicals used to create the beam. An efficient electrically powered laser is the most desirable solution for improving the magazine depth. It would create a much more easily rechargeable power source that potentially could provide a near unlimited magazine. Diode lasers have made this possible.

Diode Pumped Alkali Lasers

Diode lasers are electrically powered and can have an efficiency of up to 70%, but the power of a single diode stack is limited to around 100 Watts [5]. A method of getting kilowatts of power from a diode laser is Diode Pumped Solid State Lasers (DPSSLs). These work by combining the power of several diode laser stacks in another solid material, usualy some kind of crystal, which then lases as one high power beam. The DPSSL has problems reaching powers much higher than several kilowatts and with long term use because of heat build up in the crystal. The heating from the diodes degrades the beam quality of the crystal and eventually can damage it.

Diode Pumped Alkali Lasers (DPALs) show promise of meeting all three of the weapons grade laser criteria. The system is similar to the DPSSL, but in this case an array of diode stack lasers is used to pump an alkali gas mixed with a buffer gas. The gas then creates a single high power laser. Because the alkali is a gas, heat can be removed by simply flowing the heated gas out of the laser and replacing it, avoiding the heat build up that occurs in crystals. Also, the heated gas does not effect the beam quality as much as a heated crystal. The DPAL is electrically powered, can reach kilowatt power levels, and does not inherently degrade the beam quality. It is likely the ideal choice for a weapon grade laser system.

In the grand view of things, this thesis supports the further development and understanding of this laser system by investigating the fundamental properties of the alkali gas cesium (Cs) and its interaction with the buffer gas argon (Ar) and light.

3

Purpose and Motivation

The purpose of this experiment is to collect the absorption spectrum of the D_1 and D_2 lines of the alkali Cs perturbed by the noble gas Ar. Spectra are collected at several different temperatures and pressures to see how the spectrum in the far-wings changes. These spectra are compared with spectra predicted by two similar theories which can be used to help determine the potential energy curves of Cs perturbed by Ar.

The basic physics and concept of a DPAL is fairly simple, but to create a good weapons grade HEL all of the details are important. The motivation for this thesis is to help understand the detailed and complicated kinetics and interactions taking place in a DPAL by improving the understanding of the physics involved. Several things to consider are the complex interplay of the buffer gas pressure, the gas temperature, and the energy transfer between the alkali atoms and buffer gas that will ultimately determine the best DPAL. Theoretically, any alkali and buffer gas could be used in a DPAL. Questions that need to be answered include which alkali and buffer gas combination is best and what properties will determine the answer? To find the answers to these questions purely through experimental trial and error of every possible combination and situation would take huge amounts of time and resources. With a good enough understanding of the theoretical physics, the number of viable DPAL systems can be narrowed, giving direction and speed to finding the answers to these questions and creating a functioning high power DPAL. This thesis will contribute to the understanding of the fundamental physics of Cs - Ar interactions and further the development of the DPAL.

Overview

This thesis will first look at a basic background of the DPAL laser and then into how it works. Then it will touch on the history of the theory of line-shapes and explain it at a basic level. The experimental setup and methods will be described followed by results and analysis. Finally, a discussion of the line-shapes with respect to calculated potential energy curves is given, followed by concluding remarks.

II. Background

DPAL

In 2001, William Krupke came up with the idea of creating a DPAL in his search for a multi-kilowatt laser for industrial applications [6]. At that time, the DPSSL was already in use and sparked the idea. As has already been mentioned, the DPAL preserves the high efficiency (70%) and power (>100 watts per bar cm) of diode lasers but removes the inherent problems associated with heating the solid state gain medium of a DPSSL. It replaces this crystal with an alkali gas which can efficiently convert the energy into a single laser beam.

The DPAL system takes advantage of two very strong spectral lines in alkalies, the D_1 and D_2 lines. These lines result from the absorption or emission of a photon when the single valence electron of the alkali transitions to the first or second excited state (this ignores the hyperfine structure, discussed in Appendix B). The ground state of the alkali atoms is the $n^2S_{1/2}$ state, where n is the principle quantum number; which is 6 in the case of Cs. The first excited state is $n^2P_{1/2}$ at 1.39 eV and the second is $n^2P_{3/2}$ at 1.45 eV. Transitions between the $^2S_{1/2}$ and $^2P_{1/2}$ create the D_1 line and transitions between $^2S_{1/2}$ and $^2P_{3/2}$ create the D_2 at 8943.6 Å and 8521.2 Å wavelengths, respectively. The energy levels and transitions are pictured in Figure 1.

The diode used to pump a DPAL system is set to the D_2 wavelength to transition alkali population to the $^2P_{3/2}$ level. The degeneracy of this level is 4, while it is 2 for the ground state allowing 2/3 of the population to be moved up when in equilibrium. The population is moved down to the $^2P_{1/2}$ through collisional energy transfer with a buffer gas. If this transfer happens fast enough, then a population inversion is achieved between the $^2P_{1/2}$ and $^2S_{1/2}$ states, and a laser can be produced at the D_1 wavelength. Once inversion is created in the alkali, it can be used as the gain medium

6
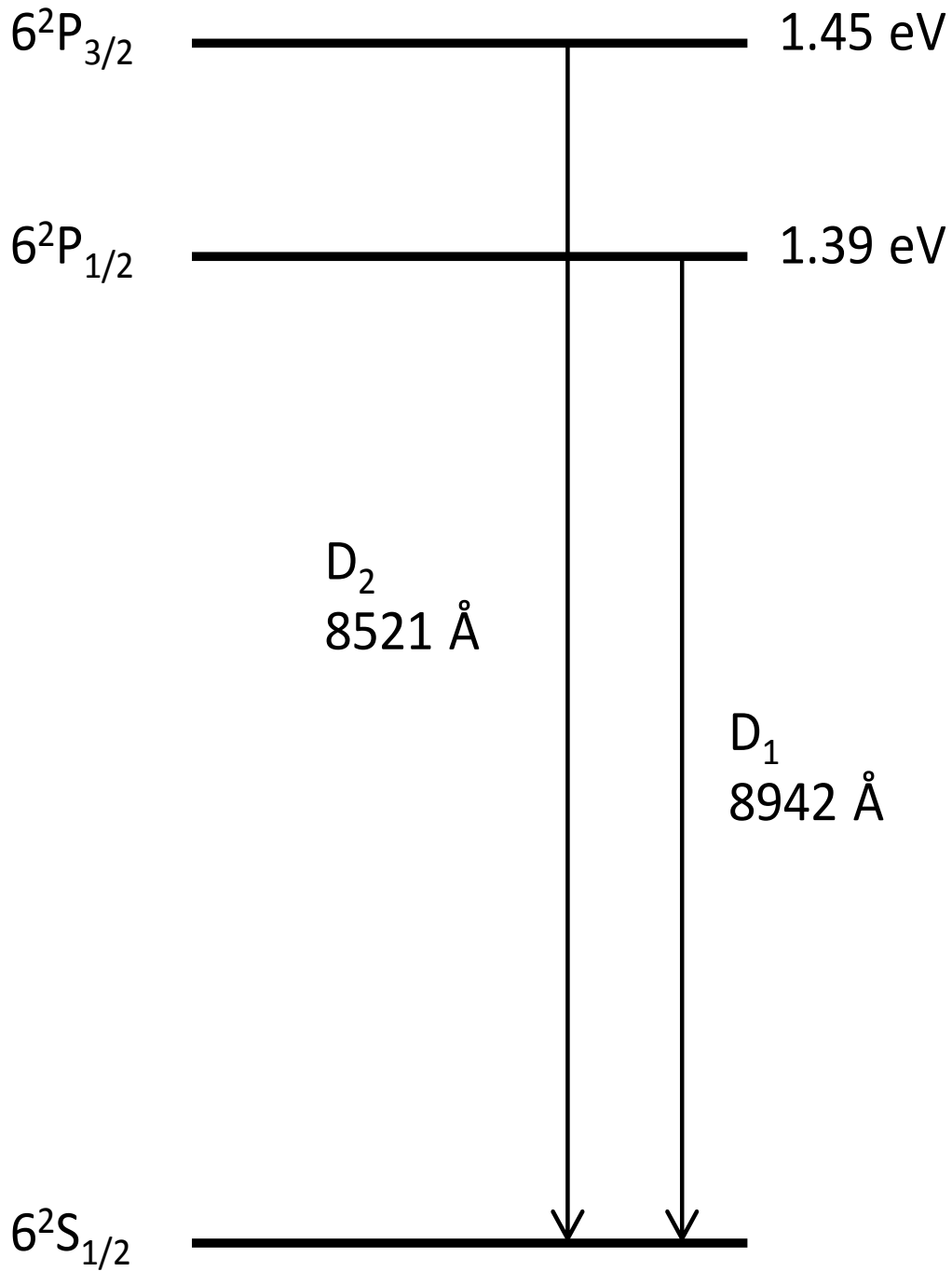
Figure 1. These are the energy levels of the Cs D_1 and D_2 transitions used in the DPAL system. Note this is not to scale.

in a laser. Studies by Glushko and Movsesyan [7, 8], more than a decade before Krupke proposed this system, have shown that an alkali gas can achieve population inversion in the presence of an appropriate buffer gas, and the concept for this pumping and lasing system was demonstrated by Beach in 2004 [9].

One reason the alkalies are an attractive choice for replacing the solid state crystals is their high quantum efficiency. The ratio in energy of the $^2P_{1/2}$ state to the $^2P_{3/2}$ state is called the quantum efficiency. For Cs it is greater than 95% and is even better for lighter alkalis. This means that if all the energy absorbed in the D_2 line is emitted on the D_1 line less than 5% of the energy would be lost. There are two other fundamental processes that contribute to the overall efficiency. One is the absorption of the diode laser light and the second is the population transfer from the $^2P_{3/2}$ state to the $^2P_{1/2}$ state. In order to efficiently absorb the diode laser light, the absorption spectrum of the alkali needs to match the spectrum produced by the diode. Also, the absorbed energy in the excited $^2P_{3/2}$ must be efficiently and quickly moved to the $^2P_{1/2}$ state. Both processes are critical to making an efficient laser.

The typical spectral bandwidth of a diode laser is ≈ 100 GHz (≈ 2Å). The absorption bandwidth of an alkali at zero Torr is ≈ 600 MHz (≈ 0.01 Å). This mismatch means that the majority of the power from the diode is not absorbed by the alkali and is lost. This absorption problem can be solved in two ways. One way is to narrow the bandwidth of the diode laser. Using volume Bragg gratings Gourevitch has reduced the bandwidth of diodes to ≈ 10 GHz and still maintained an output power of 30 Watts [10]. This width is still too broad unless the alkali is broadened by about a factor of 20. This is the second option for adjusting the bandwidths to match.

Pressure broadening is a well known method of increasing the absorption bandwidth of gases. The pressure of a buffer gas broadens the line at a rate determined by the buffer gas used. These rates have been experimentally determined for many

different buffer gases for the alkalies, and Cs in particular has recently been studied [11, 12]. The basic theory of these effects is discussed in Chapter III. The absorption bandwidth of an alkali can match the volume Bragg grating narrowed diode at pressures under an atmosphere. Pressures near 5 atmospheres are needed to match a $\approx$ 100 GHz diode. But, as alkalies are pressure broadened, very obvious but less well understood effects appear in the far wings of the absorption spectrum (or line-shape). These wing effects extend out as far as 20 nm ($\approx$ 8 THz) from the core of the line-shape and can be significant at pressures as low as 500 Torr. These wings absorb 1000 times less than the core, but for alkalies this is still significant enough to help absorb light outside the core, thus improving the efficiency of the laser.

The transfer of population from the $^2P_{3/2}$ to the $^2P_{1/2}$ level is required to produce the needed population inversion. This transfer is made possible by the buffer gas mixed with the alkali. When a molecule or atom from the buffer gas interacts with an excited alkali atom, energy can be transferred to the buffer gas moving the alkali from the $^2P_{3/2}$ to the $^2P_{1/2}$ state. When this is done quickly enough, the population in the $^2P_{1/2}$ state can exceed that in the $^2S_{1/2}$ state, creating inversion. Currently, the most efficient method to accomplish this is to use a complex molecule like ethane or methane which has many vibrational energy levels to collisionaly transfer the population of the alkali. The many close vibrational energy levels make it likely for the molecule to have an energy transition matching the $^2P_{3/2}$ to $^2P_{1/2}$ transition of the alkali when they collide. However, these chemicals slowly react with the alkalies, slowly using up the alkali in the system and creating laser snow which degrades performance [13]. A preferred buffer gas is one of the noble gases. Due to their closed valence shells, they do not react with the alkalies at all. They do not have vibrational energy levels to match to the alkali transition energy, so in general they don't transfer population as fast. If one of these gases can provide a fast enough transfer of population from the

9

$^2P_{3/2}$ to the $^2P_{1/2}$, it will be much better for a sustainable DPAL.

This work will contribute the understanding of both of the absorption of the wings of the Cs - Ar spectrum, and the rate of energy transfer between the $^2P_{3/2}$ and $^2P_{1/2}$ state. The absorption line-shape can provide useful information about how well Cs can absorb the diode laser. These line-shapes also provide information on the potential energy curves created when the Cs valence electron energy is perturbed by the presence of the Ar. Though not covered here, these potential curves determine, via quantum mechanics, the rates at which Cs atoms can transfer their energy with a given perturber. The connection between line-shape and potential energy curves is examined in this thesis in hopes of helping improve the determination of the potential energy curves in the future.

Brief Overview of Theory History

Line-shapes and their causes have been studied since at least 1895 when Michelson published his paper on line broadening [14]. The far wing line-shapes discussed in this thesis were observed as many as 80 years ago and well before the first laser [15]. In these wings there is a great deal of non-symmetric behavior as well as the presence of secondary peaks referred to as satellites. The explanation for the line-shape of these spectra has been a subject of study ever since then. The first to write a review of the subject was Weisskopf in 1933, and this work contributed mostly to the development of the core line-shapes [16]. In the following years, there were many different theories which approached the subject of creating unified line-shapes in different ways such as Frank-Condon methods or expansion methods [16]. Two theories are focused on in this thesis. The first is the quantum quasi static approach to line broadening. The first foray into quasi static methods was primarily developed in the 1930's by Kuhn and his associates based on Holtsmark's work in Stark broadening [16]. Jablonski developed

10

the theory to include quantum effects [17]. The second was primarily developed by Anderson and Talman in 1956 [16]. They put together a unified theory that is able to produce the entire line-shape of a perturbed atom. There are specialized methods for looking at different parts of the line-shape which can prove more accurate, but for a unified theory, Anderson-Talman is the best known.

III. Basic Theory

There are two predominate limits in which the theories of line-shapes are viewed. The first is the impact limit. In this limit, the perturber is assumed to interact with a radiating atom essentially instantaneously. This limit gives an excellent understanding of the core of line-shapes. The second is the static limit. Here, the radiating atom is assumed to be radiating faster than the collisions, and the perturbers can be considered to be stationary around the atom distributed by their number density. The following theories predict line-shapes in one of these two limits.

Core Line-Shapes

Core line-shapes describe the spectrum very close to the unperturbed frequency of an atomic transition. The primary components are Doppler broadening, pressure broadening, and natural broadening. The last two can be put in the category of homogeneous broadening because both effect every atom in a system in the same way. Natural broadening comes from the Heisenberg uncertainty principle, $\Delta E \Delta t \geq h$. The fact that excited states do not last forever inherently produces a certain amount of uncertainty in their energy. This uncertainty creates a line-shape that is given by a Lorentzian

$$g(\nu) = \frac{\gamma}{2\pi\left[(\nu - \nu_0)^2 + (\gamma/2)^2\right]}, \tag{1}$$

where γ is the FWHM of the line, ν_0 is the line center and ν is the frequency [18, p. 160ff].

Pressure broadening in the core of the line works in the impact limit. It assumes that the radiation of an atom or group of atoms can be treated as a classically radiating wave at a given frequency which decays exponentially with some lifetime. Collisions with buffer gas atoms typically occur in a much shorter amount of time

12

but the impacts are not quite instantaneous. The spectrum produced by taking into account the impact effects is the same Lorentzian shape as Equation 1 with a couple of changes:

$$g(\nu) = \frac{\gamma}{2\pi \left[(\nu - \nu_0 - \sigma)^2 + (\gamma/2)^2\right]}. \tag{2}$$

The FWHM, γ, now increases with increasing perturber pressures, $\gamma = R_p P$, where R_p is the pressure broadening rate, P is the pressure, and σ is a pressure induced shift in the center frequency [16].

Doppler broadening goes in the category of inhomogeneous broadening because it does not affect each atom in the same way. This broadening, as the name suggests, is the result of the Doppler effect. An atom moving toward an incoming photon will see a slightly blue shifted frequency, while an atom moving away will see a red shifted one. The distribution of wavelengths is then dependent on the distribution of velocities of the atoms, given by the Maxwell-Boltzmann distribution

$$\frac{\mathrm{dN}}{N} = \left(\frac{M}{2\pi k_b T}\right)^{1/2} \exp\left(-\frac{M v_z^2}{2 k_b T}\right) \mathrm{d}v_z \tag{3}$$

where $\frac{dN}{N}$ is the fraction of atoms moving in the z direction with velocities between v_z and $v_z + dv_z$, M is the mass of the atom, k_b is the Boltzmann constant, and v_z is the velocity in the z direction. In general, the line-shapes can be described by the contribution of the Lorentzian at each speed, given by the integral [18, p. 170]

$$g(\nu) = \left(\frac{M}{2\pi k_b T}\right)^{1/2} \int_{-\infty}^{\infty} \left[\frac{\gamma}{2\pi \left[\left(\nu - \nu_0 + \nu_0 \frac{v_z}{c} - \sigma\right)^2 + (\gamma/2)^2\right]}\right] \exp\left(-\frac{M v_z^2}{2 k_b T}\right) \mathrm{d}v_z. \tag{4}$$

This is the Voigt line-shape and accounts for both homogeneous and inhomogeneous effects. When the Lorentzian is extremely narrow in comparison to the distribution

13

of the speeds the Gaussian shape dominates, and the line-shape is given by

$$g(\nu) = \left(\frac{4\ln 2}{\pi}\right)^{1/2} \frac{1}{\Delta D} \exp\left[-4\ln 2\left(\frac{\nu - \nu_0}{\Delta D}\right)^2\right] \qquad (5)$$

where

$$\Delta D = \nu_0 \left(\frac{8k_b T \ln 2}{Mc^2}\right)^{1/2}. \qquad (6)$$

ΔD is called the Doppler width [18, p. 171].

The Doppler broadening does contribute to the shape of the Voigt which is important to getting accurate line-shapes. But it does not have a large effect at high pressures, because pressure broadening dominates. The Voigt is very accurate around the line-shape core. The shape holds, even at high pressures in the core but additional theory is needed to account for the shape of the wings.

Quantum Quasi Static Approximation

One of the most basic explanations for spectral satellites is in the quasi static limit which looks at the radiation distribution from a statistical view-point [16]. Assume that all the perturbing atoms are stationary and distributed in a volume around a perturbed alkali atom based on number density. The frequency of a given photon absorbed by the alkali will depend on the difference in energy levels of the ground state and the excited state. The energy levels are perturbed by what is assumed to be one atom, and depend on the distance, R, between the alkali and the perturber. The probability of radiating at a frequency in a range from ω to $\omega + d\omega$ is the probability of finding an atom at the distance R to $R + dR$ which corresponds to the energy difference of that frequency. These are related by

$$\omega_0 + \Delta\omega = (E_i - E_f)/\hbar = \omega_0 + \Delta V/\hbar, \qquad (7)$$

14

where E_i and E_f are the perturbed energy levels, or potential energy curves, of the radiating atom and depend on R, the atomic separation of the alkali and perturber [16]. ΔV is the difference of those two energy levels minus the unperturbed energy difference $(\Delta V_0 = \omega_0 \hbar, \ (E_i - E_f) = \Delta V_0 + \Delta V)$.

The intensity for a given frequency is proportional to the probability of finding a perturber in the region R to $R + \mathrm{d}R$, which corresponds to the potential difference for that frequency [16]. $4\pi R^2 \mathrm{d}R$ is the volume of the spherical shell between R and $R + \mathrm{d}R$. This equation multiplied by n, the concentration of perturbers, is the probability of finding an atom in that range in the static limit. This means $I(\Delta\omega)$ is related by

$$I(\Delta\omega)|\mathrm{d}\omega| \propto n4\pi R^2 |\mathrm{d}R|. \tag{8}$$

Solving for $I(\Delta\omega)$, this becomes:

$$I(\Delta\omega) \propto n4\pi R^2 \left| \frac{\mathrm{d}\omega}{\mathrm{d}R} \right|^{-1}, \tag{9}$$

which using Equation 7 becomes

$$I(\Delta\omega) \propto n4\pi R^2 \left| \frac{\mathrm{d}\Delta V}{\mathrm{d}R} \right|^{-1} \hbar. \tag{10}$$

This shows the explicit relationship between the line profile predicted by $I(\Delta\omega)$ and the inverse of the derivative of the difference potentials. The derivative of the difference potential is of course zero at local minima and maxima and the predicted intensity goes to infinity at these points. This is obviously unphysical, but it does create a spike at locations other than the core of the line.

The potential energy curves of these interactions are the deciding factor in determining the frequencies of the radiation. These can be determined directly by solving the many body quantum mechanical problem involving all the electrons in both the

15

alkali and perturbing atom along with their respective nuclei. The solution to this complicated problem can only be approximated numerically and has been attempted by Blank [1] for alkalies perturbed by noble gases. The results presented by Blank for Cs and Ar are plotted in Figure 2. When the potentials are formed by the presence of two atoms, the states are labeled using molecular state labels. For alkalies, the ground state, which unperturbed is the $^2S_{1/2}$, becomes $X^2\Sigma^+_{1/2}$, the $^2P_{1/2}$ becomes the $A^2\Pi_{1/2}$, and the $^2P_{3/2}$ splits into two states, the $A^2\Pi_{3/2}$ and $B^2\Sigma^+_{1/2}$.

Figure 3 is a plot of the difference potentials for each of the excited states with respect to the ground state. According to Equation 7, the plotted difference potentials show the possible frequencies allowable for a transition, from the core of the line out to several Angstroms on each side. The minimum in the difference potential of $B^2\Sigma^+_{1/2}$ in Figure 3 clearly produces a spike at ≈ 820 nm, the calculated location of a blue satellite based on these potential surfaces and this theory.

Some of the quantum mechanics involved can be taken into account to give a more realistic prediction. For a given frequency (or wavelength) there are only certain atomic separations that give a difference potential which corresponds to that frequency; these atomic separations are called Frank-Condon points (R_c). There can be more than one Condon point for a given frequency depending on the difference potential. Equation 10 must be evaluated at each of these points and summed to get the total $I(\Delta\omega)$. The Boltzmann distribution determines the number of atoms available to transition at the energy given by R_c. For the case of absorption this is governed by the potential curve of the ground state. Lastly, the probability of a transition actually taking place is determined by the dipole interaction of the two states. This is simply the transition dipole moment

$$\left\langle X^2\Sigma^+_{1/2}\right| D \left|A^2\Pi^+_{3/2}\right\rangle, \tag{11}$$
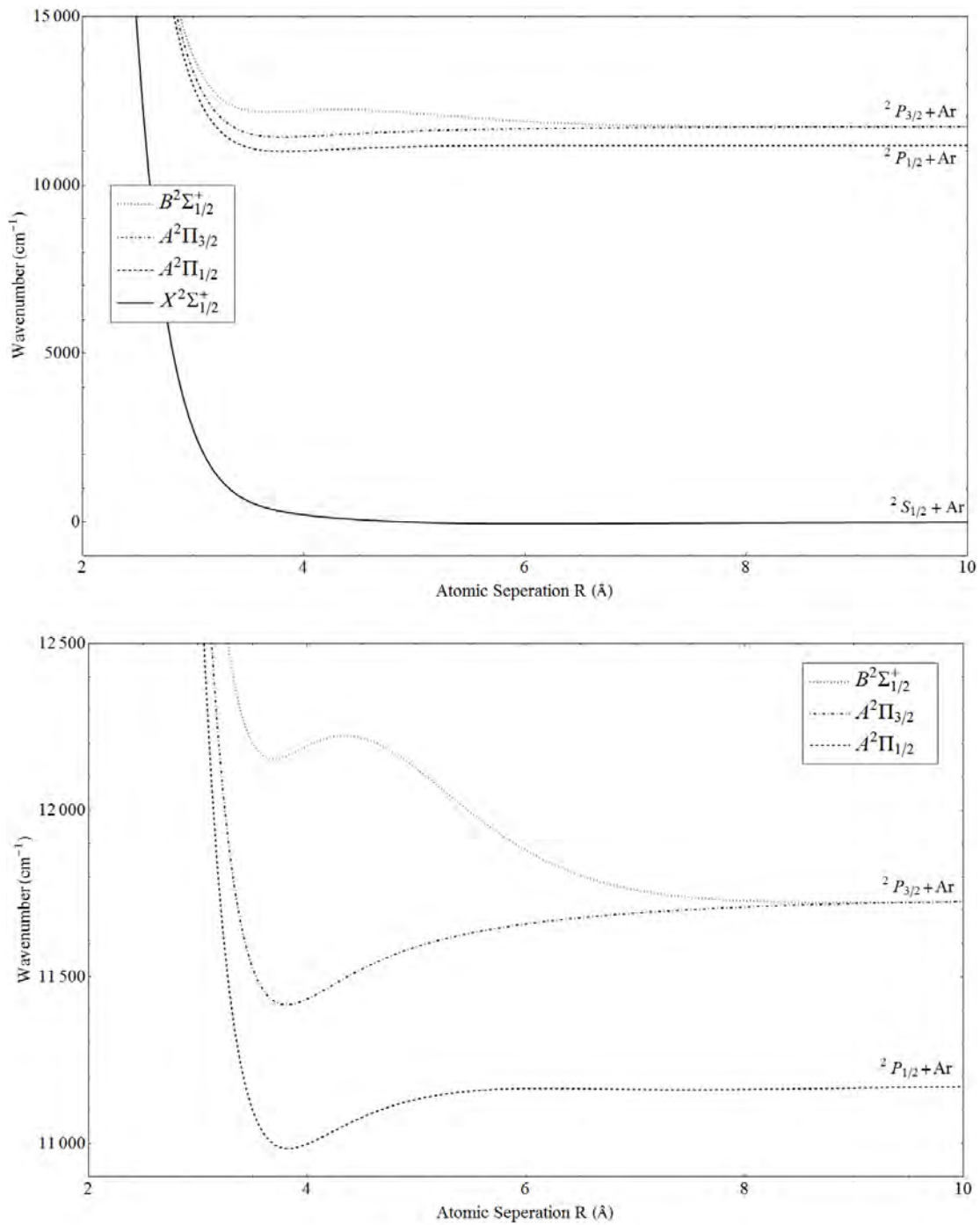
16

Figure 2. The potential surfaces of Cs perturbed by Ar as calculated by Blank [1]. Top: All four curves $X^2\Sigma^+_{1/2}$, $A^2\Pi_{1/2}$, $A^2\Pi_{3/2}$, and $B^2\Sigma^+_{1/2}$. Bottom: A closer view of $A^2\Pi_{1/2}$, $A^2\Pi_{3/2}$, and $B^2\Sigma^+_{1/2}$ curves, revealing their shape.
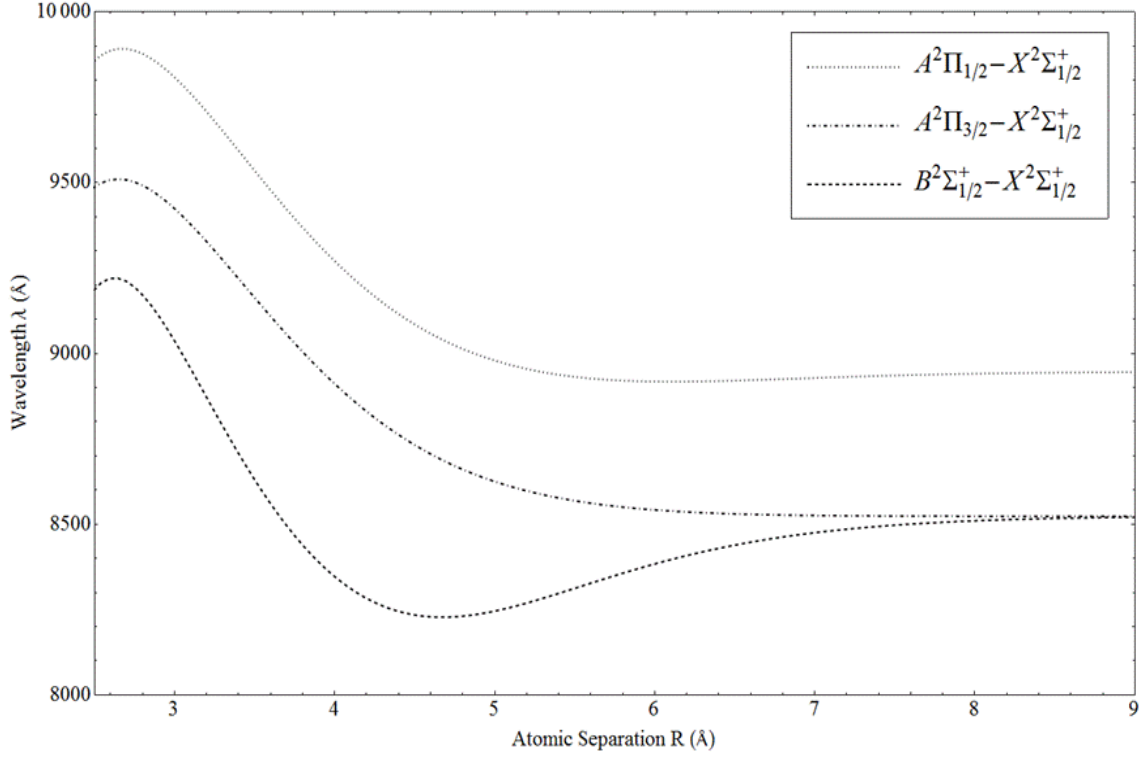
17

Figure 3. The difference potential curve between each upper curve $A^2\Pi_{1/2}$, $A^2\Pi_{3/2}$, and $B^2\Sigma_{1/2}^+$ and the ground state curve $X^2\Sigma_{1/2}^+$, used to theoretically predict the line-shape of the D_1 and D_2 spectra.

where D is the dipole operator. The absolute value squared of Equation 11 gives the expectation value, represented by $|\mathrm{D}(R_c)|^2$ and depends on R_c because each potential surface also depends on R_c. The dipole moments are also determined quantum mechanically and were calculated for these potentials by Blank and are shown in Figure 4. All these pieces together give the quantum quasi static approximation to the line-shape:

$$I(\omega) \propto \sum_c R_c^2 \left| \mathrm{D}\left(R_c\right) \right|^2 \left| \frac{\mathrm{d}(\Delta V)}{\mathrm{d}R} \right|_{R_c}^{-1} \times n_{\mathrm{Ng}} \exp\left(-\frac{X^2\Sigma_{1/2}^+\left(R_c\right)}{k_B T} \right) \qquad (12)$$

where n_{Ng} is the number density of the noble gas. This still produces a spike at the core and blue peak but gives a more realistic prediction for the wings. The D_1 and D_2

18
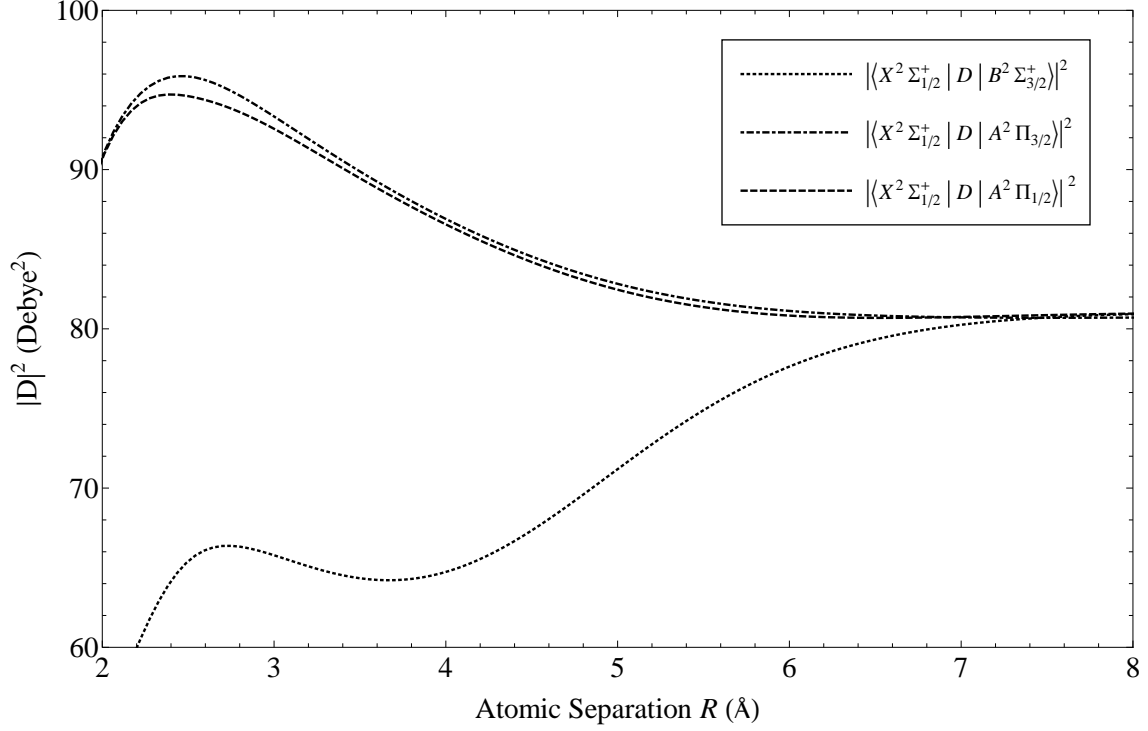
Figure 4. The squared transition dipole moment of $X^2\Sigma^+_{1/2}$ with each of $A^2\Pi_{1/2}$, $A^2\Pi_{3/2}$, and $B^2\Sigma^+_{1/2}$. It accounts for the quantum probability of a transition taking place between the respective levels.

spectrum is predicted using this equation and is compared with the collected spectra in Chapter VI.

Anderson-Talman

A more complete theory is present in the Anderson-Talman method [16]. The Anderson-Talman theory does not give as clear a relation between the physics and the math due to how it deals with averaging all the different possible effects, but is able to produce the core of the line-shape as well as satellite and wing features.

This line-shape is formed from the Fourier transform of what is called the autocorrelation function. The autocorrelation function (Φ) is a measure of the phase and frequency change created by perturbers acting on a radiating alkali. The following

19

equations show the full calculation.

$$\Phi(s) = \exp(-ng(s)) \tag{13}$$

with

$$g(s) = 2\pi \int_0^\infty b\,\mathrm{db} \times \int_{-\infty}^\infty \mathrm{d}x_0 \left[1 - \exp\left(-i \int_0^s \hbar^{-1} V \left[(b^2 + x^2)^{1/2} \right] \mathrm{dt} \right) \right] \tag{14}$$

where

$$x = x_0 + \bar{v}t, \tag{15}$$

The autocorrelation function is calculated by taking the exponential of the function $g(s)$ times the number density of perturbers, n. $g(s)$ is a function that accounts for the changing phase and frequency of a radiating alkali. $\int_0^s \hbar^{-1} V \left[(b^2 + x^2)^{1/2} \right] \mathrm{dt}$ is the phase term determined by the difference potential and the location of the perturber over the time from $t = 0$ to $t = s$. $g(s)$ accounts for all possible collision by integrating over all possible paths given. Due to the cylindrical symmetry of the problem, these paths can be put in terms of b, the impact parameter, and x, how far an atom moves in a given amount of time t, where $\bar{v}$ is the average velocity of the perturber gas and x_0 is the starting location. The integration assumes that the trajectories of the perturbing atoms are straight, which is not true. But, in the summation which is being performed, an averaging of many different trajectories is occurring and the theory still works. s is related to what part of a collision is accounted for; if s is large the major contribution to the integral is when the perturber is far from the alkali, when s is short the major contribution is from perturbers that are close. In general, $g(s)$ is a rapidly oscillating function near $s = 0$ that becomes a straight line asymptotically as s increases. $\Phi(s)$ takes all the factors in $g(s)$ and includes the number density of perturbers. All together $\Phi(s)$ accounts for all of the effects of a

20

perturbing gas on an atom, when the Fourier transform is performed, the line-shape is produced.

The impact limit of Anderson-Talman is found when $s \to \infty$. This can be thought of as taking into account longer collision paths of a perturber as s gets longer. For $s \to \infty$ the effects of a perturber that has come from some x_0, has gone infinitely far away, it simply collided and left. This means the primary contribution from ΔV is when it is near the unperturbed energy, or in the core. When $s \to \infty$, according to Allard and Kielkopf [16], $g(s)$ can be written as

$$g(s) = (\alpha_0 + i\beta_0) + (\alpha_1 + i\beta_1)s. \tag{16}$$

This is simply a straight line. α_0 and β_0 are constants typically chosen to be zero but can contribute asymmetry in the core if calculated. If the autocorrelation function's contribution is primarily an exponentially decaying straight line, given by (13) and (16), the line-shape produced is Lorentzian, both shifted and broadened. The α_1 gives the Lorentzian line width and β_1 gives the line shift [16].

The static approximation of Anderson Talman theory takes the limit in which the perturbers are stationary, or $\bar{v} \to 0$. When $\bar{v}$ is set to zero, Equation 14 simplifies. The difference potential is evaluated at a given radius R and the integrals over db and dx_0 become an integral over dR. For $\bar{v} \to 0$, $x \to x_0$ and $b^2 + x^2 \to R^2$, so

$$g(s) = 2\pi \int_0^\infty b\mathrm{d}b \int_{-\infty}^\infty \mathrm{d}x_0 \left[1 - \exp\left(-i \int_0^s \hbar^{-1}\Delta V \left[R\right] \mathrm{d}t \right) \right], \tag{17}$$

which further simplifies to

$$g(s) = 4\pi \int_0^\infty R^2 \mathrm{d}R \left[1 - \exp\left(-i\hbar^{-1}V(R)s \right) \right]. \tag{18}$$

This allows a much more easily calculated integral that can be done analytically, depending on the potentials. In this limit the major contributions to $g(s)$ are from perturbers close to the alkali and ΔV is far from the un-perturbed value, so this most accurate in the wings. Additionally, for small values of s, $g(s)$ is rapidly oscillating. These oscillations, when Fourier transformed, becomes a secondary maximum in the wing of the core or the satellite.

The concentration of the perturber in Φ plays a role in determining the best approximation limit to use. The larger n is from Equation 13, the more quickly the exponential goes to zero. When n is small, i.e. low pressure, the asymptotic portion of $g(s)$, large s, has a large contribution to the Fourier transform because the exponential does not die out very quickly. The impact approximation is best for low pressures. But when n is large, i.e. high pressure, the exponential goes to zero quickly and the major contribution to the Fourier transform is from the oscillating portion of $g(s)$, small s. The static limit is best for high pressures.

Overall, Anderson-Talman theory predicts a much more physically acceptable line-shape than the quantum quasi static. It does not go to infinity at any point and predicts both the core line-shape as well as the satellite and wings. The general form will not be used here, but the static limit will be used to predict a line-shape for the Cs - Ar absorption spectrum and compared to measured spectra. The measured spectra have high concentrations of Ar so the static limit is a good choice. Spectra predicted by this theory will also be compared to measured spectra in Chapter VI.

Beer's Law

Intensity of light is what is typically measured in an absorption experiment. The theories just discussed deal with the shape of the line. The line-shape and intensity

are related by Beer's Law,

$$I(\lambda) = I_0 \exp(-NL \; \sigma(\lambda)), \tag{19}$$

where I_0 is the intensity before absorption, N is the concentration of absorbers, L is the path length through the absorber, and $\sigma(\lambda)$ is the cross section of absorption.

$$A(\lambda) = -Ln\left(\frac{I}{I_0}\right) = NL \; \sigma(\lambda) \tag{20}$$

is the absorbance. $\alpha(\lambda) = N\sigma(\lambda)$ is the coefficient of absorption. These are both proportional to the line-shape and Absorbance ($A(\lambda)$) is used here because it simply depends on I and I_0. Another useful quantity is the reduced absorption coefficient (k), given by

$$k(\lambda) = \frac{\alpha(\lambda)}{[N_a][N_b]}, \tag{21}$$

where $[N_a]$ is the alkali concentration and $[N_b]$ is the perturber concentration. The theory of line-shapes has been developed to the point of being able to predict unified lines from the core to the wing and the locations of satellite peaks. Both the quantum quasi static approximation and Anderson-Talman in the static limit can predict wing line-shape. The satellite peaks can be found using the basic $1/\mathrm{d}\Delta V = 0$ concept, though it results in line-shapes that go to infinity. Anderson-Talman can avoid this. The actual height of the satellite peak in relation to the peak of the core line is important to know, and is predictable via Anderson-Talman.

> It should therefore be possible to investigate the potential function of the interaction of two atoms ... experimentally by measuring the intensity curve towards the wings of the broadened lines.

> - Kuhn, 1934

23

The line-shapes of observed atomic absorption spectra are what this theory is trying to match. Their primary use is to help determine the potentials surfaces of the interaction of two atoms. This will be successful when the potential surfaces are accurate and the theory is correct. The following experiment will help reach this goal.

IV. Experimental Methods

Overall Setup

This experiment looks at the far wing absorption spectrum of Cs perturbed by Ar. In order to do this, high concentrations of Cs were desired as well as high Ar pressures. The intent was also to see how the spectrum changed with Cs concentration and Ar pressure, in order to accomplish this an experimental apparatus was set up in the following manner. A broad band Ealing lamp with an Oriel Instruments 68831 power source was used to illuminate vapor phase Cs contained in a heat pipe in order to observe the absorption lines. Two lenses were used to collimate the light through the heat pipe. After passing through the heat pipe, a mirror was used to direct light around a 90 degree turn and then through an $f/\#$ matched lens into a monochromator. The light was detected using a photomultiplier tube (PMT) with a PC collecting and recording the data. The monochromator was scanned from 8300 Å to 9200Å collecting the spectrum for both the D_1 and D_2 absorption lines.

Heat Pipe

The heat pipe allows the Cs concentration ([Cs]), and buffer gas concentration to be controlled and easily changed by adjusting the temperature of the pipe and the buffer gas pressure contained in the pipe. The heat pipe used here was built by Charles Fox as part of [19]. Brewster's angle windows were attached to either end of a pipe approximately 1 inch in diameter. The inside of the heat pipe had a wire mesh held around the inside edge of the pipe by a stiff coiled wire. A heater block consisting of two pieces of aluminum was attached to the center of the heat pipe with eight electrode heating elements placed inside along with two thermocouples for reading the temperature. Two Watlow temperature controllers would control the
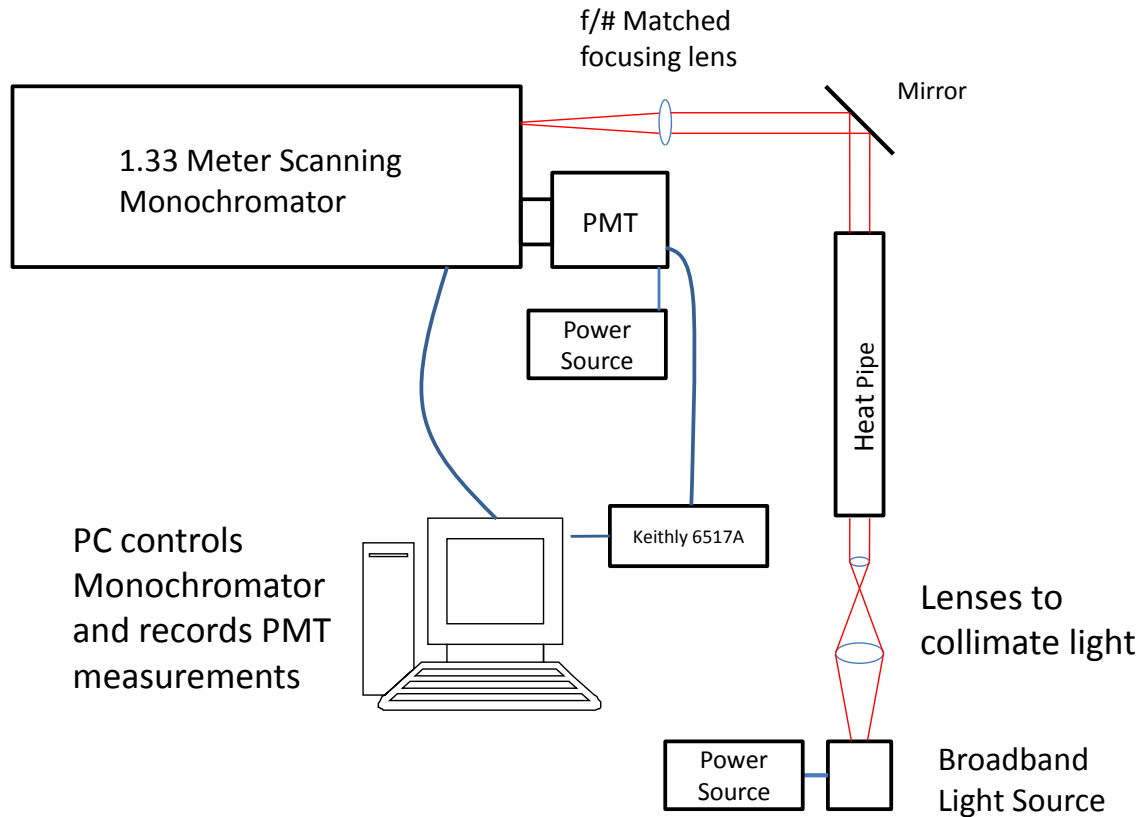
25

Figure 5. Experimental Apparatus Setup.

current in the electrode elements using the feedback from the thermocouples to hold
the temperature at the desired level. The cooling blocks on either end were connected
to two water coolers, one for each side, keeping the temperature in these regions below
the melting temperature of Cs. A detailed description of the heat pipes construction
can be found in Fox's lab notebook [20]. The heat pipe is divided into three regions,
a heated region in the center and two cooled regions on either end. Figure 6 shows
the basic structure and function of a heat pipe. The Cs in the hot section melts
and evaporates creating a vapor filled region, the vapor moves outward to the cool
region where it condenses and falls to the bottom of the pipe the wire mesh allows
the Cs to wick along the length of the heat pipe back to the hot region. This region
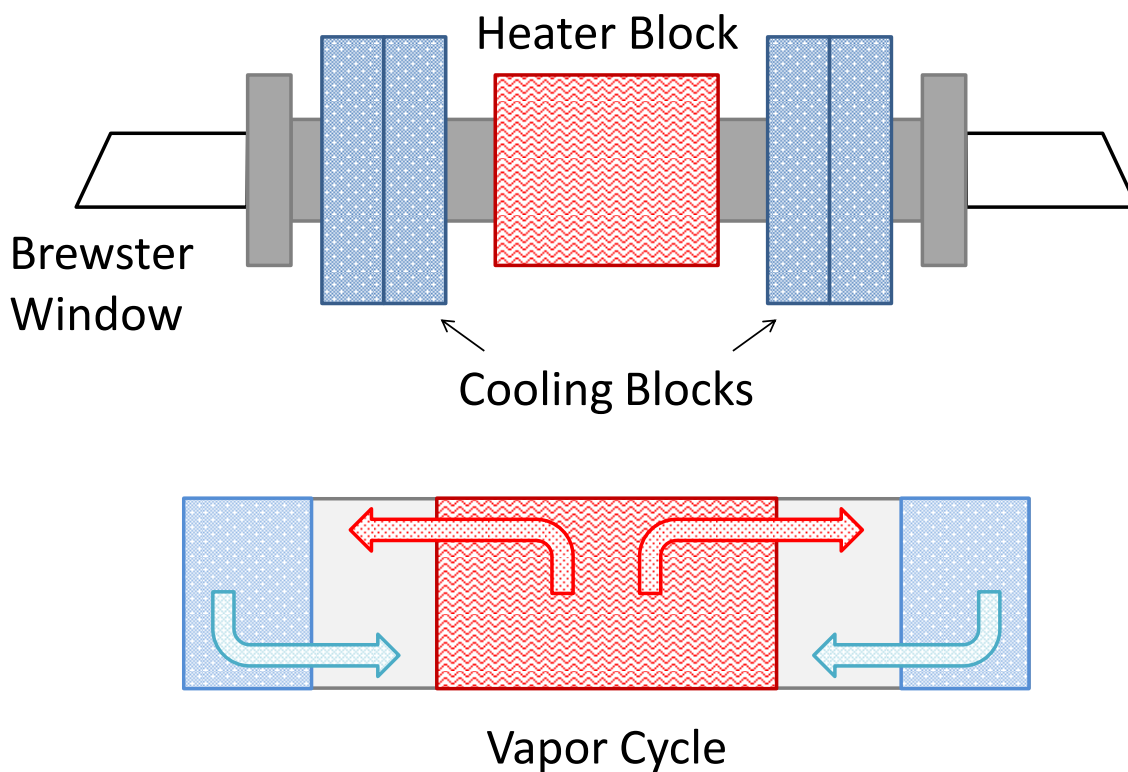is considered to contain the Cs vapor when the pipe is being heated; the distance

26

Figure 6. **Top is a diagram of the heat pipe showing heated and cooled regions. Bottom shows the flow of Cs vapor inside the pipe.**

between the middle of the cooled regions was 17 cm for this heat pipe.

Attached at each end of the heat pipe was a valve connected to the gas handling system, used to control the buffer gas pressure. An MKS Barometer was used to measure the pressure of the buffer gas and an Alcatel vacuum pump was used to empty the cell of gas when needed. All together, this keeps a steady Cs concentration in the heat pipe at a controllable pressure and temperature without the Cs sticking to the windows and obstructing observation.

Monochromator

The monochromator was a 1.33 m McPherson 609, installed with a 1200 gr/mm grating giving an observable wavelength range of 1850 Å to 13000 Å. The monochro-

mator was scanned using a Compumotor stepper motor and driver connected to a PC. At a slit width of 10 μm the resolution of the monochromator was 0.1 Å. The Burle C31034 PMT was powered by a Stanford Instruments High Voltage power supply set at 1325 V for a 10 μm slit. The PMT had a dark noise of about -3.2 nA and a near linear response over the range of the D_1 and D_2 lines. The PMT current was read using a 6517A Keithley electrometer controlled by the PC.

Data Acquisition

A PC controlled both the Keithly electrometer and the monochromator stepper motor. A Virtual Instruments© program was created to step the motor and read the PMT current to collect the spectrum data. The temperature of the heat pipe, internal buffer gas pressure, Ealing lamp, and PMT HV were all controlled independently. All the data collection runs presented here were done with a slit size of 10 μ, a PMT HV of 1325, and a lamp current of 7.70-7.75 Amps.

The wavelength-axis was calibrated using the D_1 and D_2 lines which are very well known [21]. At each buffer gas pressure, two scans were done at room temperature, well under the melting point of Cs. Even at this temperature there was enough Cs absorption to see the two absorption lines. These were used to calibrate the x-axis using a linear fit of the two points (greater detail is given in Appendix D). The step for the motor was set such that the x-axis interval was 0.1 Å. Spectra from 8300 Å to 9100 Åwere collected for each scan and took approximately 4.5 hours, collecting about 8000 data points.

Using the discussed apparatus, 80 spectra were collected. The Ar pressure in the heat pipe was set at the desired level and then eight spectra were collected. Two spectra were collected with the heat pipe at room temperature and six were collected where the pipe heater was set to temperatures of 50 °C to 175 °C in steps

28

Table 1. Collected Spectra Heat Pipe Conditions

Pressure(Torr)	Temperature(°C)
100	20
200	50
300	75
400	100
500	125
748	150
1124	175
1504	
1884	
2280	

of 25 °C. In order to reach 175 °C the heater block was set as high as it would go, so the temperature would go over 175 °C by a few degrees. Because the Cs concentration is what is desired for calculations and the actual temperatures recorded would vary slightly, the Cs concentration is what is reported, the set temperature is just a reference for which spectrum was collected. Spectra for this set of heat pipe temperatures were collected for each of 10 Ar pressures listed in Table 1.

V. Results & Analysis

Determining I over I_0

In order to extract the line-shape from collected data, Equation 20 must be used to calculate absorbance $A(\lambda)$. A typical raw data spectrum, I, collected for a given scan is shown in Figure 7, the natural Log of I divided by I_0 must be calculated in order to obtain A. The best way to obtain I_0 is concurrently as you obtain I, but this was not done for this experiment primarily because a second spectrometer would have been needed. Instead, I_0 was obtained by collecting a spectrum with the heat pipe at room temperature. This ensured the heat pipe had as little gas phase Cs in it as possible, an example of I_0 is shown in Figure 8. The overall shape of the data collected is determined by both the black body spectrum of the Ealing lamp and the photo cathode resposivity of the PMT, which begins to drop off at about 8500 Å. These are simply scalar factors on the actual intensity which apply both to the I scans and I_0 scans. When the ratio of I to I_0 is taken, these effects cancel out. The dark current of the PMT was the only additive effect and was subtracted from both lines.

A significant problem faced in the analysis of this data was that each absorption spectrum collected seemed to sit on a different I_0. The intensity, at wavelengths known to be outside the absorption spectrum, was changing in value between scans (see Appendix C). This was primarily caused by the Cs vapor becoming a "fog" for certain concentrations and Ar pressures. Because this effect was scalar, dividing I/I_0 would remove such effects but the scaling factor was not the same for both spectra. In order to get an accurate absorbance spectrum, an I_0 consistent with the measured I was needed.

At each Ar pressure two I_0 spectra were collected. A 50th degree polynomial was

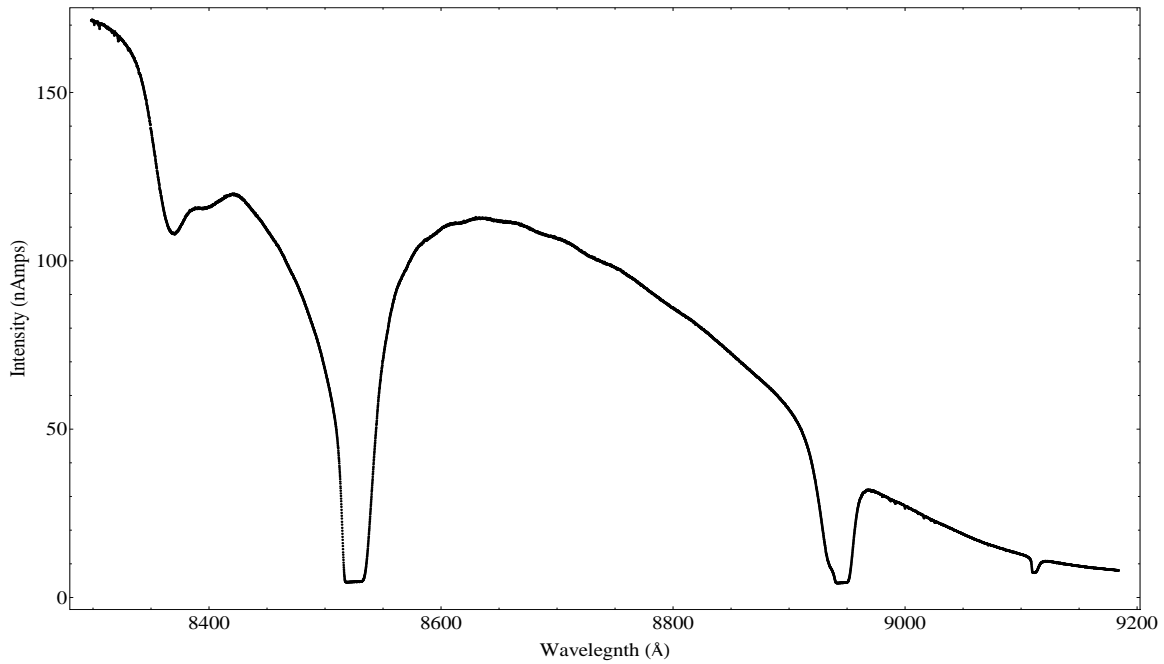**Figure 7.** A typical spectrum, I, before dividing by I_0. This was collected at an Ar pressure of 1124 Torr and a [Cs] of 9×10^{14} cm^{-3}. The scan is from 8300 Å to 9100 Å with an interval of 0.1 Å, for about 8000 data points.
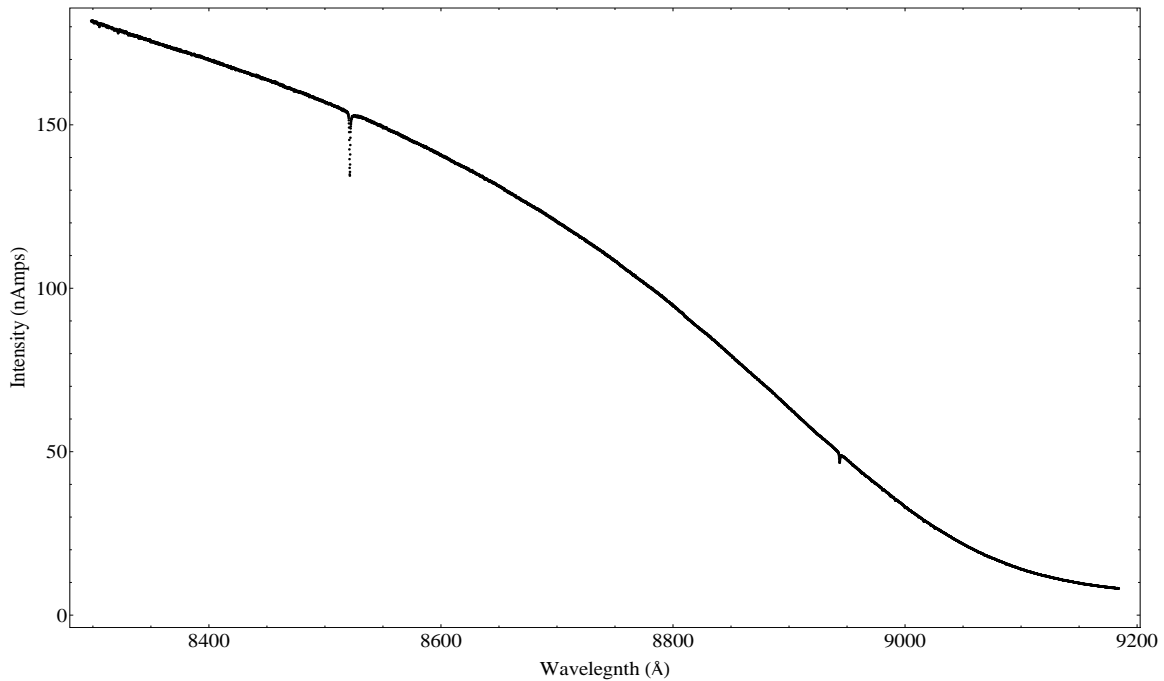

Figure 8. This is a typical I_0 spectrum collected at room temperature. As can be seen here, there is still a small amount of absorption and the D_1 and D_2 lines. These peaks were used to scale the x-axis.

31

fit to each pair of I_0 spectra collected. This gave a good estimation ($R^2 > .999$) of the I_0 spectrum over the desired range. These two polynomial functions were slightly different from each other and were used as the basis functions for a linear combination fit of the very far wings of I. The spectrum measured at a heat pipe temperature of 175 °C was always fit first because it had the fewest data points at wavelengths not effected by the large amount of absorption. When a good fit to this spectrum was obtained the data corresponding to the same wavelengths would be used to fit the spectra taken at lower temperatures. This would provide a minimum of data points to use in the fit, for I spectra that did not have as much absorption. This was repeated for each set of spectra collected for each Ar pressure.

Once I_0 was determined for an I spectrum the absorption was calculated from Equation 20. From $A(\lambda)$ the cross section, $\sigma(\lambda)$, can be calculated using the length of the heat pipe containing cesium, L, and [Cs]. Figure 9 shows the spectra collected at 1124 Torr of Ar pressure and [Cs] from 6.7×10^{11} to 9.4×10^{14} cm-3. Figure 10 shows the spectra for Ar pressures from 100 to 2800 Torr and a Cs concentration of around 6×10^{14} cm^{-3}, Appendix A presents all of the data collected.

Determining Cross Section & Reduced Absorption Coefficient

The cross section ($\sigma(\lambda)$) and reduced absorption coefficient (k) are the most fundamental values that can be determined from these spectra because they are independent of Cs concentration ([Cs]) and absorption path (L). k also removes the dependency on Ar concentration ([Ar]) determined by the pressure. Because of this the spectra collected at the same pressure should give the same $\sigma(\lambda)$.

[Cs] and L can be difficult to determine, but parameters of the heat pipe provide a basis for the calculation. [Cs] can be calculated from the vapor pressure of the Cs for a given temperature. The cooling blocks confine the Cs vapor and the distance

between them is L. But neither of these are direct measurements and many unknown factors can effect them, such as temperature gradients inside the heat pipe and the pressure of the Ar.

[Cs] and L multiplied together give a simple scaling factor to $\sigma(\lambda)$ and k (Equation 20). This factor, [Cs]L changes for each spectrum depending on the Ar pressure and heat pipe temperature. By plotting parametrically with respect to wavelength, the absorbance of the spectrum taken at one temperature versus one taken at another, a straight line should be produced. The slope will be the ratio of $\frac{[\text{Cs}]L_y}{[\text{Cs}]L_x}$, the subscripts denoting which axis the absorbance is plotted against. Figure 11 shows the result of plotting the absorbance in this way for all the spectra collected at 748 Torr.

Using the slopes determined in this way, a value for [Cs]L could be determined accurately for spectra taken at very temperature as long as [Cs]L was known for one
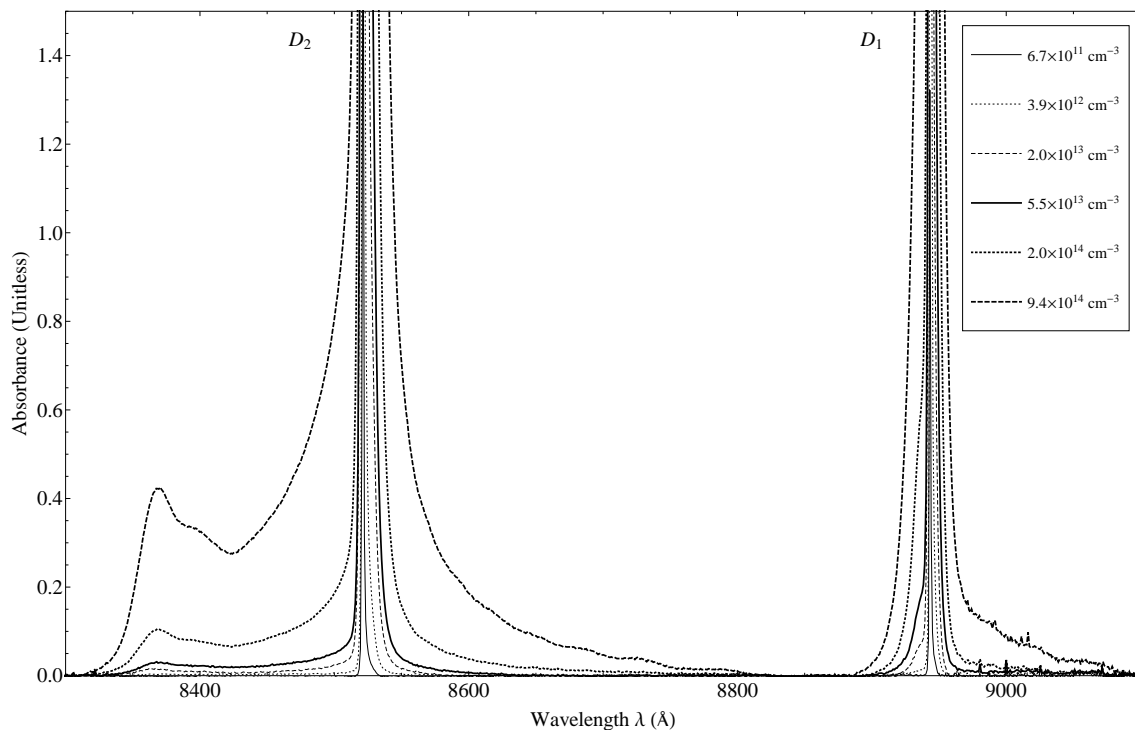
Figure 9. The measured absorption spectrum at 1124 Torr for Cs concentrations from 6.7×10^{11} to 9.4×10^{14} cm^{-3}.
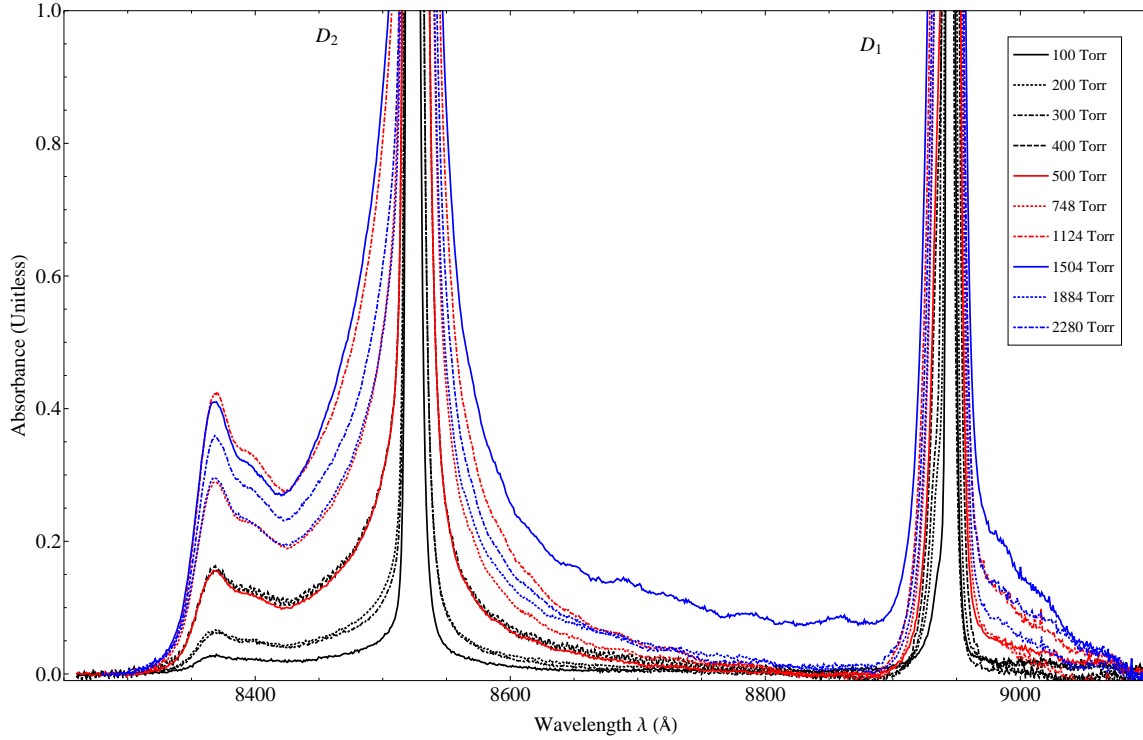
Figure 10. The absorption spectrum for all pressures measured (100 - 2280 Torr) at about the same Cs concentration, $\approx 6 \times 10^{14} \text{cm}^{-3}$.

of them. The uncertainty of [Cs] increases with increasing temperature as does the approximation of L. To minimize the error $[Cs]L$ was calculated for the spectrum collected at 50 °C using the measured temperature, Cs vapor pressure curve, and a length of 17 ± 0.5 cm. The calculated $[Cs]L$ values were then used to calculate $\sigma(\lambda)$ and k for each spectrum.

Because the intensity spectrum depends on the exponential of $[Cs]L\sigma(\lambda)$, low temperature spectra captured the core of the line-shape without loss of shape from the Cs becoming opaque at that wavelength. High temperature spectra did become opaque and cut off the core, but the spectrum of the far wings shows up clearly. Combined, the data at each temperature for a fixed pressure created a full spectrum $\sigma(\lambda)$ line-shape. The 1124 Torr $\sigma(\lambda)$ is shown in Figure 12.
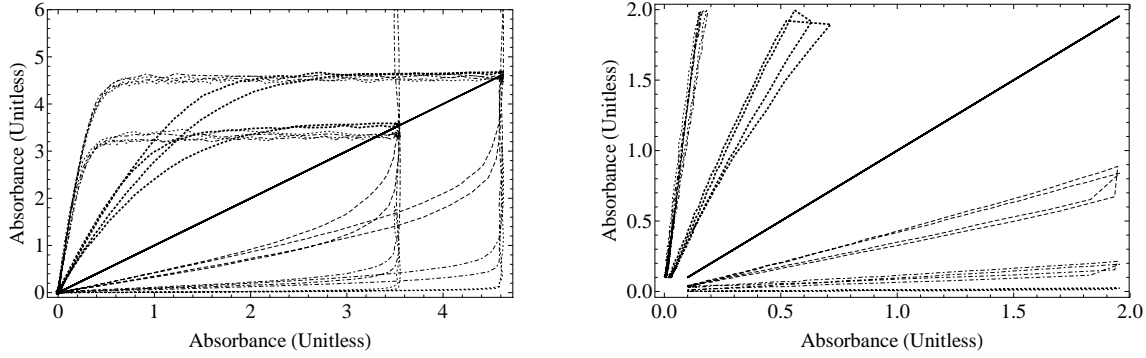
Figure 11. These two plots show how the ratio of one absorbance spectrum is proportional to another at a given pressure. The data shown here is at 748 Torr for each measured [Cs], the lines to the right and bottom of the reference line have a smaller [Cs]L coefficient while those to the left and top have a greater [Cs]L. [Cs]L is calculated in the regular way for a reference line and from that all the others can be determined.

Uncertainties

In a heat pipe, the length containing Cs vapor is not well defined because the Cs is prevented from reaching the windows by the cooling blocks. There is some length inside the heat pipe that is filled with circulating Cs but where it starts and ends is difficult to determine. The best estimate was a measurement of the distance between the centers of the cool regions of the heat pipe, 17 ± 0.5 cm, which directly contributes to the uncertainty in the calculated $\sigma(\lambda)$.

Figure 13 shows the vapor curve of cesium for a given temperature. The line is given by

$$\log_{10} P_v = 2.881 + 4.165 - \frac{3830}{T} (\text{ liquid phase}) \tag{22}$$

from [21], where P_v is the vapor pressure of Cs and T is the temperature. There were two temperatures measured for each spectrum collected using thermal couple probes. These could be different by as much as 15 °C, but the purposes of this report the average temperature was used to calculate the vapor pressure using Equation 22 and the Ideal Gas Law was used to determine a Cs concentration. The temperatures were
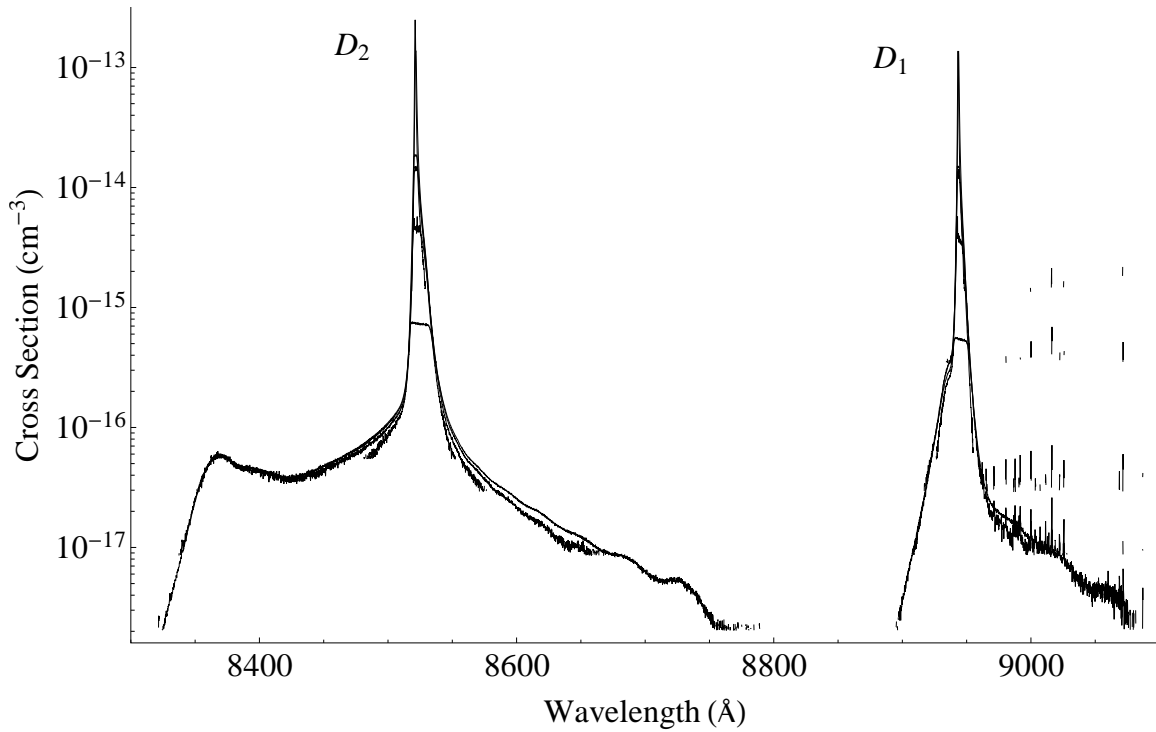
35

Figure 12. The approximate cross section of both the D_1 and D_2 line created by plotting together the $\sigma(\lambda)$ calculated from spectra collected at different [Cs] at an Ar pressure of 1124 Torr. The log scale shows the detail of the blue and red satellite as well as the peak of the core.

measured from the outside of the heat pipe with the probes placed on the surface of the heat pipe, well inside the heater block, so they give an accurate temperature of the heater block, but the temperature inside the heat pipe may be different, increasing the uncertainty. From this, the uncertainty in the concentration is about 25%. This, along with L mentioned above, was used for the 50 °C spectra in order to get a reference [Cs]L for a given pressure.

The fluctuations in [Cs] (see Appendix C) caused subtle and gradual changes over the course of a scan and the line-shape would be changed. This is most obvious looking at the $A(\lambda)$ vs $A(\lambda)$ plots in Figure 11. The uncertainty from bad fits was typically isolated and the data was disregarded, the [Cs] drift created an uncertainty of 2% in the slopes of A vs A plots.
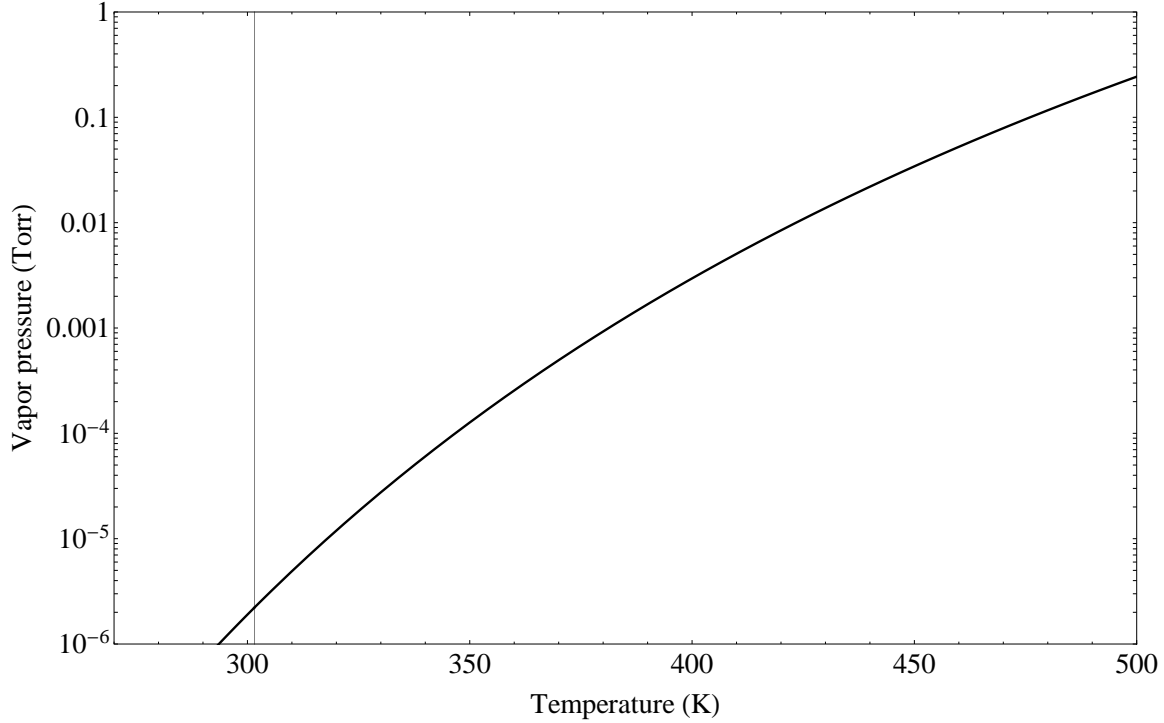
Figure 13. This is the vapor pressure curve of Cs over the range used in this experiment. The vertical line shows the melting temperature of Cs.

Figure 14 shows the reduced absorption coefficient, k, of the wing line-shape measured in these experiments along with that reported by Readle [13]. This k was calculated using a 748 Torr pressure scan with a [Cs] of 7×10^{14} cm^{-3}. As can be seen the values measured here tend to be two times greater. The uncertainty is as high as 50%. The conbined uncertainty of [Cs], L, and the [Cs]L slope contributes to this. Also the method used to find these values of k was introduced near the end of this study and they were not found to be consitant for different pressures as they should have been indicating a high uncertainty in the measurement. This would likely be greatly improved by using even lower temperatures to determine the refernce [Cs]L used to find these values.

The uncertainty in calculated absorbance values $A(\lambda)$, comes from two sources, the calculation of I_0 and fluctuations in [Cs] over the course of the run. Some predicted I_0
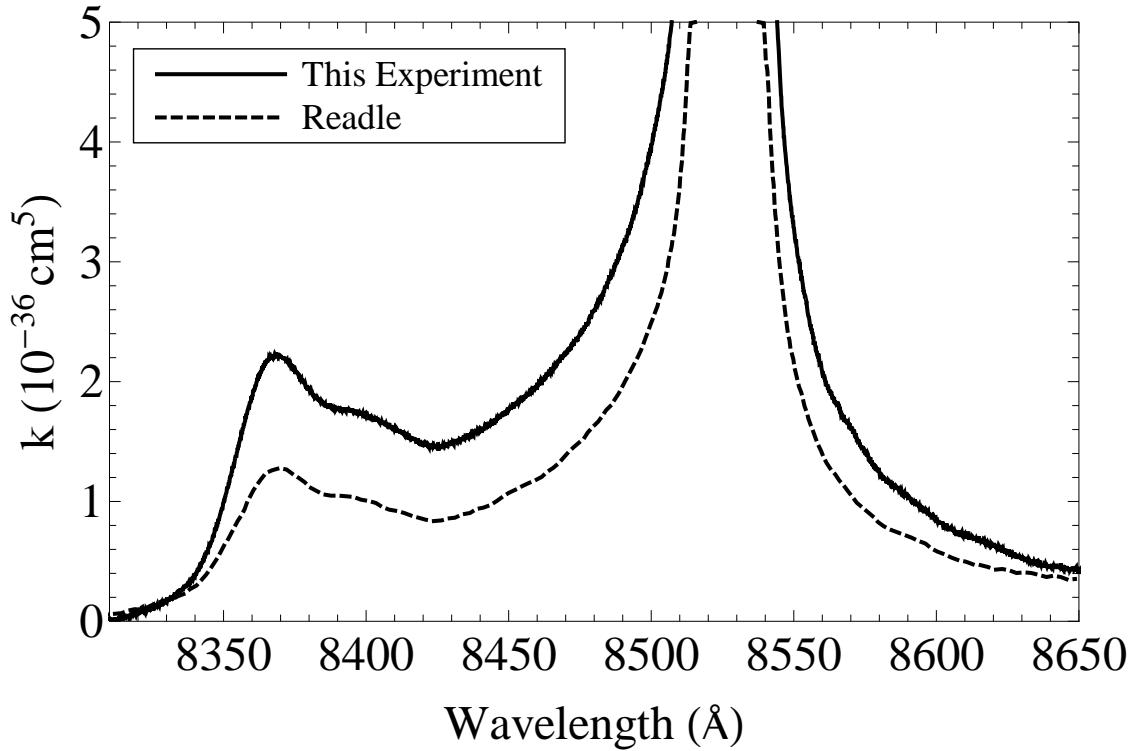
Figure 14. The calculated $k(\lambda)$ measured at 748 Torr and a [Cs] of 7×10^{14} cm^{-3}, focused on the D_2 line wings, compared to Readle's [13]. The estimated uncertainty is 50%.

spectra would have intensity values less than the measured I for certain wavelengths. When this happened, if there was no absorption in the center of the spectrum, more fit points would be used at wavelengths between the D_1 and D_2 absorption lines. This would usually define the line well enough that it would fit. There are also cases where the predicted I_0 is to high. For good fits, the uncertainty of A was ± 0.01. But the fits were occasionally bad, this was determined by comparing the absorbance spectra with each other; Figure 15 shows an example of a spectrum produced by a bad fit.

The small peaks seen to the red of the D_1 line (Figure 10 and Figure 9) are absorption features from the water in the air. Depending on the humidity these lines would be stronger or weaker. The lines were checked with a spectrum created from the HITRAN database (see Figure 49 in Appendix D). These provided a secondary check of calibration. They were used to make sure the x-axis motor positions directly
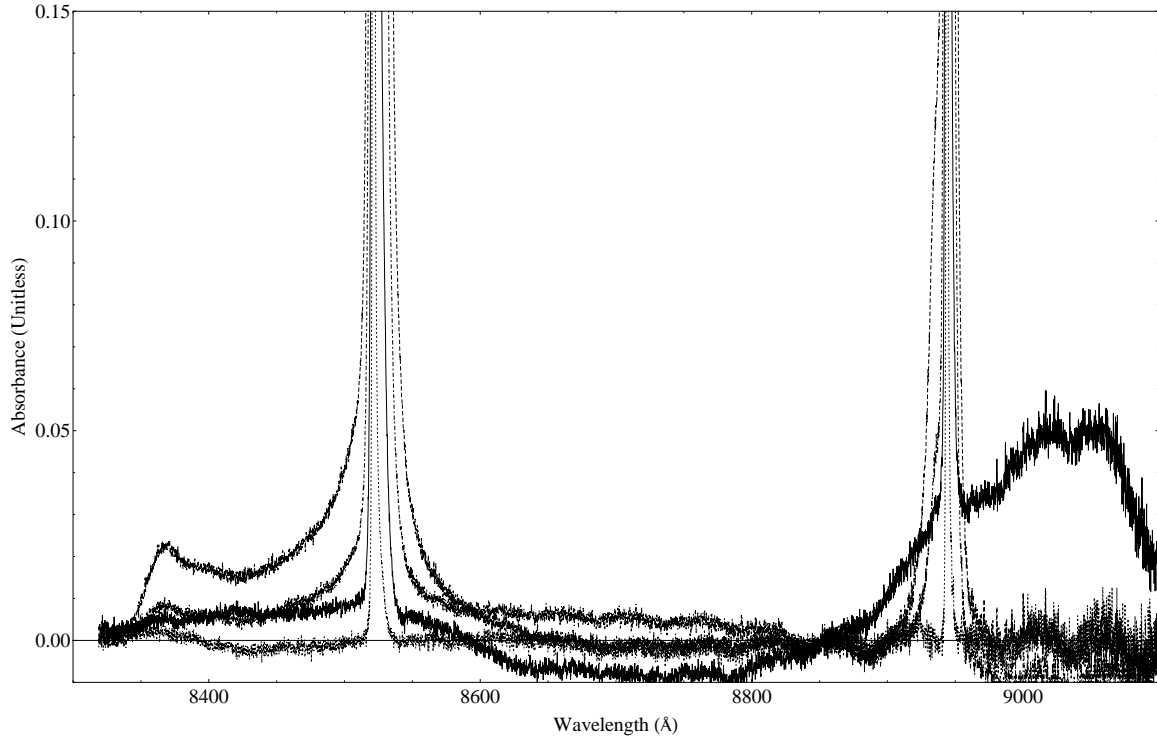
Figure 15. This set of spectra was collected at 748 Torr at several [Cs]'s. The spectra in solid black is clearly not following the trends of the others and has extreme positive and negative values where they should be zero. Such spectra are created by bad I_0 fits but typically are easily identified and ignored.

recorded for a scan were not shifted off from the x-axis values of the I_0 scan used to scale the wavelength axis. These lines are not nearly as strong as the low temperature D_1 and D_2 lines and were not used for actual calibration described in the experiment setup. The motor position locations of the D_1 and D_2 peak values could shift as much as 200 to 300 units between scans, corresponding to an uncertainty of ± 0.4 Å.

Monochromators impose a fairly large instrument line-shape on data they collect. The instrument line-shape of this monochromator was investigated by looking at the Cs D_1 and D_2 line at zero pressure. The measured line-shape was characteristic of the instrument line-shape due to the narrowness of the un-broadened Cs line. The FWHM of the instrument line-shape was ≈ 13.6 GHz (≈ 0.3 Å). At 100 Torr and a Cs concentration of 7×10^{11} cm^{-3}, the FWHM of the measured spectrum was ≈ 16.5

39

GHz ($\approx$ 0.4 Å). This indicates that there was a significant effect on the measured line-shape in the core, but in the wings where the line becomes much wider (from red wing to blue wing $\approx$ 230 Å), the instrument line-shape can be disregarded. Because the main focus here is on the wings this effect was not removed; a fuller discussion can be found in Appendix B.

VI. Discussion

The core line-shapes given by the Voigt profile have well-understood physical meanings and describe the observed line-shapes well in the core. But in the far wings the symmetry is broken and satellite peaks are observed. The quantum quasi static approach and static limit of Anderson-Talman theory were developed in order to understand and predict the wings of the line-shapes collected here. The quantum quasi static approach is used to determine where the satellites should be by simply looking for minimum or maximum in the difference potentials. It is also useful for predicting the far wing shape in certain regions. The core and satellite shapes are not accurate because the $1/d\Delta V$ nature of Equation 12 dominates around these points. The static limit of Anderson-Talman theory is able to predict both the core and wings of the line-shape. The static limit is used because the calculation is easily done given the potentials taken from Blank. Also the static limit deals primarily with highly perturbed line-shapes and their wings. In the following discussion, the spectra collected in this experiment are compared to the spectra produced by these theories from Blank's calculated potentials.

D2

The spectrum of the D_2 line has two prominent features, the far extended red wing and the blue satellite (Figure 17). The line-shape is produced by both the $A^2\Pi_{3/2}$ difference potential and the $B^2\Sigma_{1/2}^+$ difference potential. The red wing asymmetry is the dominating factor for lower Cs concentrations. The line is seen to start spreading out to the right even at Cs concentration less than 10^{12} cm^{-3}. It continues to dominate the line-shape until Cs concentrations of $\approx 10^{14}$ cm^{-3} are reached. At this point the blue wing and satellite become more prominent, with a greater absorption, and the

41

red wing simply extends much farther out than the blue wing.

The red wing is related primarily to the $A^2\Pi_{3/2}$ difference potential while the $B^2\Sigma^+_{1/2}$ difference potential is related to the blue (plotted in Figure 3). The $A^2\Pi_{3/2}$ potential surface does not have a shoulder so the difference potential shifts only to the red side of the spectrum. The $B^2\Sigma^+_{1/2}$ potential surface does have a shoulder and the $B^2\Sigma^+_{1/2}$ difference potential shifts mostly to the blue side of the core and has a minimum that creates the blue peak. The $A^2\Pi_{3/2}$ difference potential does not have a maximum in its curve before the Boltzmann factor, from Equation 12, effectively goes to zero, and shifts red slowly. This would not indicate a large red wing. But the transition dipole moment (plotted in Figure 4) for the $A^2\Pi_{3/2}$ is larger than the transition moment of the $B^2\Sigma^+_{1/2}$. In addition the $B^2\Sigma^+_{1/2}$ difference potential does have a slight red shift before the blue peak, which is also predicted by Readle [13]. This contribution is possibly what is being seen in the cross section, Figure 12, as broadening very near the core of the line to the red side when combined, these two factors are likely the cause of the early and quick rise of the red wing. As the Cs concentration increases, the red shift near the core simply blends in. At this point, the cross section of the red wing is less than that of the blue and the blue satellite and they become the dominate features.

The peak location of the blue satellite was determined using Table Curve© to fit a peak function to the data. The fit peak's line center was taken to be the peak location. The average value from all spectra for each pressure is presented in Table 2 and show that the wavelength does not change with pressure. The uncertainties given are the standard deviations of all the measurements at that pressure.

One important relationship between the coefficient of absorption in the blue satellite and the concentrations of Cs and Ar is mentioned by Readle in his dissertation

Table 2. D$_2$ Blue Peak Center Wavelength

Pressure(Torr)	Center Wavelength(Å)
500	8369.6±0.5
760	8369.0±0.8
1140	8369.1±0.3
1520	8369.1±0.5
1900	8368.5±0.6
2280	8369.3±0.4

[13]. It is

$$\alpha(\lambda) \propto [N_a][N_b] \tag{23}$$

where $[N_a]$ and $[N_b]$ are the concentrations of the Ar and Cs respectively. This relation comes from the fact that we are assuming two body collisions. Considering Equation 12 the spectrum for one Cs atom is proportional to the Ar concentration, [Cs] would scale the spectrum for multiple Cs atoms as Equation 23 indicates. By dividing both sides of Equation 23 by the Cs concentration the relation becomes

$$\sigma(\lambda) \propto [N_a]. \tag{24}$$

Both of these equations imply that the blue peak should grow linearly with pressure. This trend was difficult to check directly because of the uncertainty in [Cs] and L. These variations were mitigated by taking the ratio of the maximum cross section in the blue peak to the cross section of the core peak for each pressure. These values are plotted in Figure 16. The linear trend is followed fairly well from 100 Torr to 1524 Torr. This expected if it is assumed the fundamental interaction is not changing but only how often it occurs. But for pressures beyond this, the relation ceases to hold in this data. There are a couple possible causes of this. One is that at this pressure the behavior of the gases inside the heat pipe stopped confining the Cs between the

43

cooling blocks. The Cs began to accumulate visibly outside the cold regions of the heat pipe at high pressures. Thus during measurements where this happened some of the Cs population was consistently being lost and L was 2 to 3 times longer. The cross section measurements mostly accounted for this by using the combined $[Cs]L$ calculation discussed in Chapter V. The other possibility is that at these pressures the approximation is no longer valid because three body interactions become important. Hedges indicates that at Ar concentrations higher than 2×10^{19} cm^{-3} these effects could start to become significant and at 1900 Torr the Ar concentration is over double this value [22]. But if this were the case a corresponding change in the line-shape would also be expected and this is not indicated in the spectra; therefore it is more likely a result of how the Cs vapor was changing.
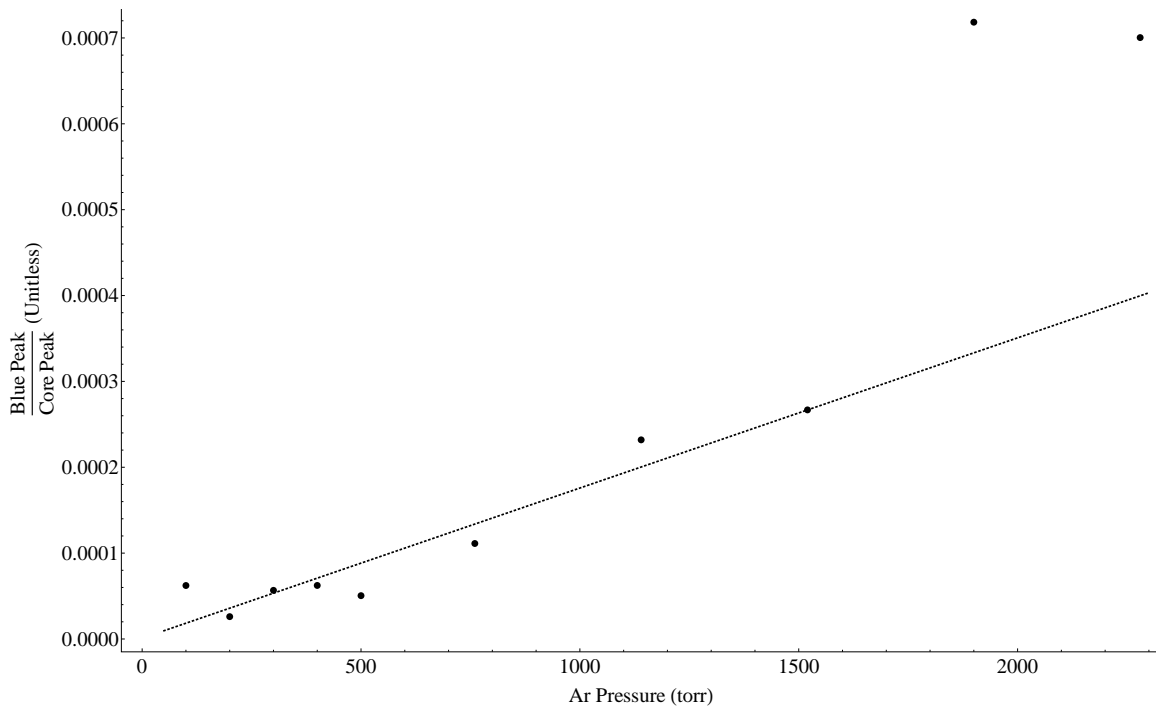
Figure 16. This shows the calculated ratio $\frac{\text{Blue Peak}\sigma(\lambda)}{\text{Core Peak}\sigma(\lambda)}$ plotted vs. Ar pressure. A linear trend is expected in the data, using the points for pressures less than 1504 Torr a linear fit was found; slope: 1.75×10^{-7}, intercept: 8.83×10^{-7}

44
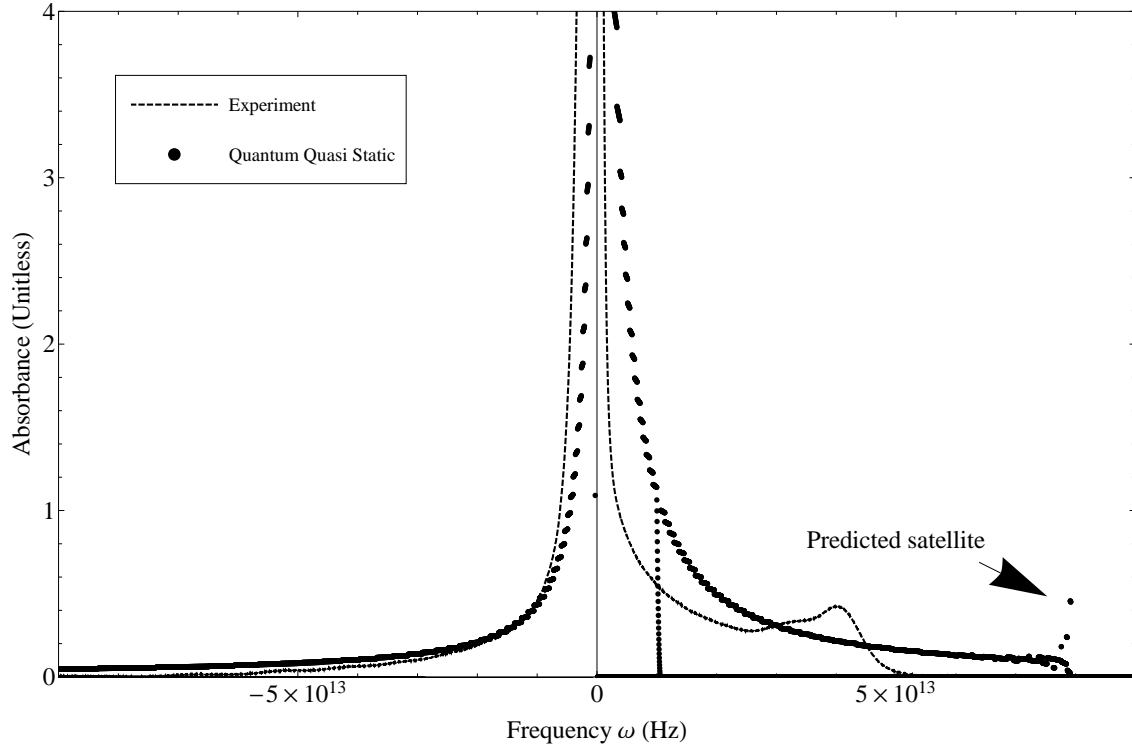
Figure 17. The line-shape and blue peak predicted by quantum quasi static theory (Equation 12) compared to measured data for D_2. The measured data was for an Ar pressure of 1124 Torr and $[Cs] \approx 9.4 \times 10^{14}$ cm^{-3}.

The line shape produced by quantum quasi static theory using both $B^2\Sigma^+_{1/2}$ and $A^2\Pi_{3/2}$ difference potential surfaces, is plotted in Figure 17. The spectrum was calculated for each surface separately then simply added together and arbitrarily scaled for the plot. It gives some indication of the line-shape between the core and blue peak and to the red side of the core. The red wing is created purely from $A^2\Pi_{3/2}$ because the Boltzmann population is very quickly going to zero, beginning at an atomic separation of $\approx$ 4 Å, damping any contribution $B^2\Sigma^+_{1/2}$ might have had in the red and the slight red rise of the difference potential is not significant for these predicted surfaces. This theory can not predict line-shapes into frequencies that do not contain Franck-Condon points, so to the blue side of the blue satellite there is no calculated line-shape.

45

The location of the blue peak predicted by the quantum quasi static method from Blank's potentials is two times farther blue shifted. The blue peak predicted by the minimum in the $B^2\Sigma_{1/2}^+$ difference potential is determined by the shoulder in the $B^2\Sigma_{1/2}^+$ potential energy curve and it is in this shoulder that the Blank potentials have the most error [1]. In the red wing of the line the shape and extent of the predicted spectrum matches much better. There are no peaks in this side of the line and essentially only one Frank-Condon point that contributes to a given frequency, these properties avoid many of the complications of the equation, making it a straightforward and fairly accurate prediction.

The static limit Anderson-Talman spectrum was produced using the $A^2\Pi_{3/2}$ and $B^2\Sigma_{1/2}^+$ and then scaled, just as it was for the quantum quasi static and is shown in Figure 18. The concentration, n, was set to 2.4×10^{19} cm^{-3}, to match an Ar pressure of 1124 Torr. The mean time between collisions at 455 K and this pressure for Ar is 480 ps. If this time was used for s, $\Phi(s)$ does not go to zero quickly enough for the discrete Fourier transform used to perform the calculation and create a good spectrum because the function gets artificially chopped off. To compensate for this a time of 5 ns was used for s. This indicates that the static approximation is not the best choice for this system, but this was expected for this pressure. The spectrum produced is very oscillatory so a moving median over 10 points was used to smooth the data, the general shape of the line and location of the blue satellite can be seen. Experimentally the blue satellite is ≈ 1000 times smaller than the core peak and the predicted blue peak is ≈ 500 times smaller than the core.

D1

The major feature observed in the D_1 line is the blue shoulder. This shoulder has a higher absorption than the blue peak of the D_2 line and the cross section is about
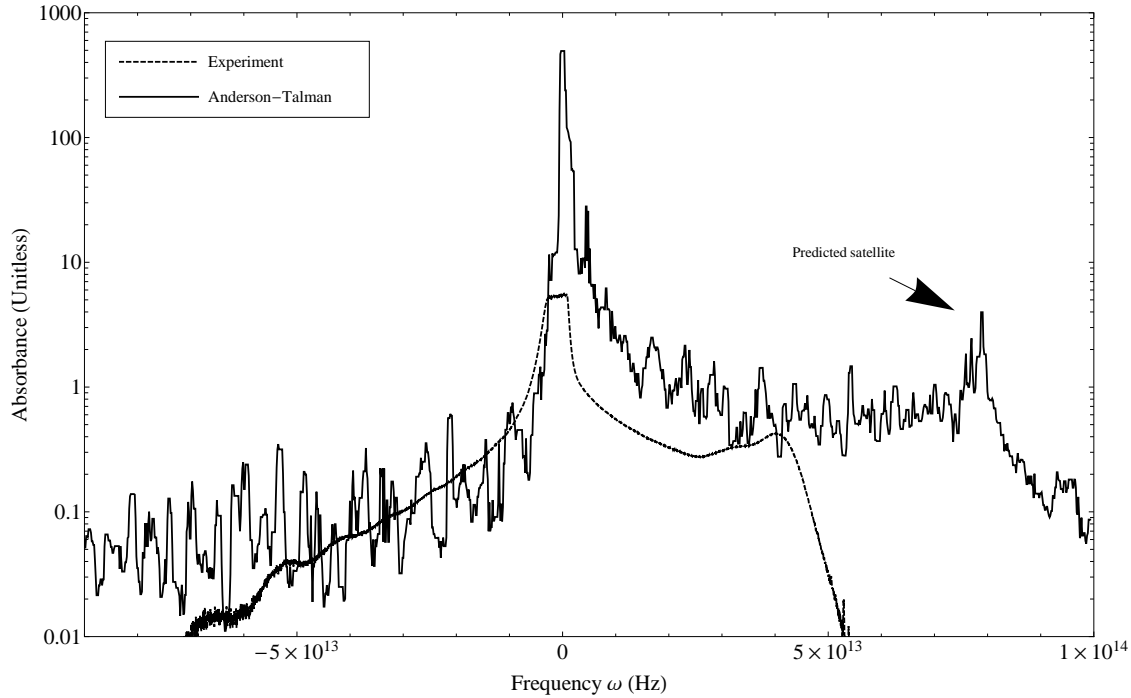
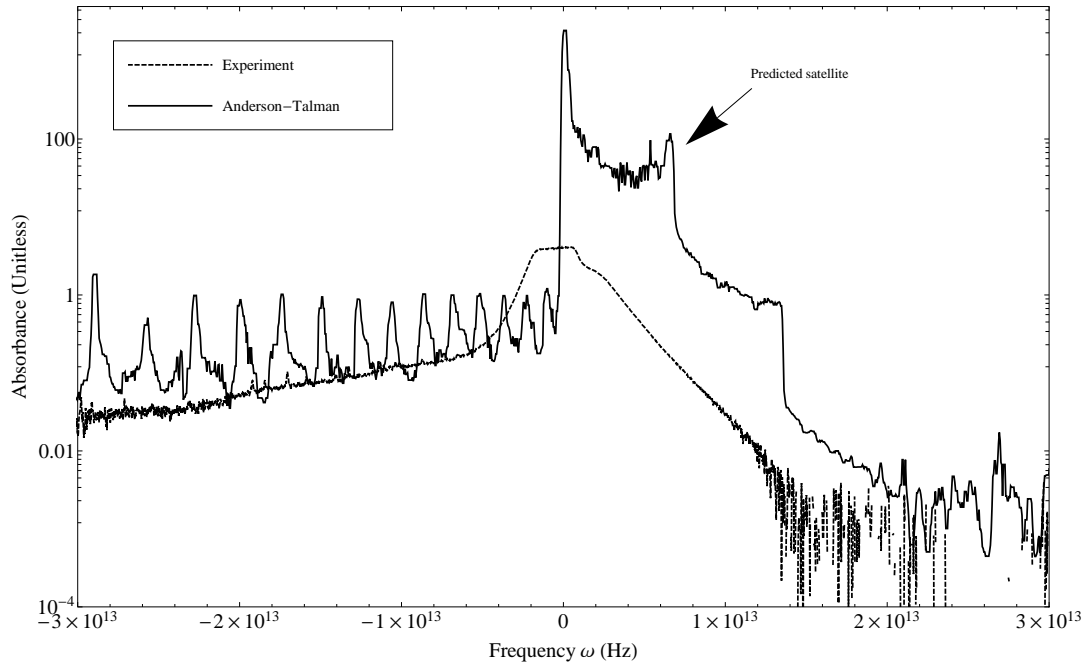**Figure 18.** The line-shape and blue satellite predicted by Anderson-Talman theory compared to measured data for D_2. The measured data was for an Ar pressure of 1124 Torr and $[Cs] \approx 9.4 \times 10^{14}$ cm^{-3}. There is a significant amount of ringing from the discreet Fourier transform used to predict the spectrum. A moving median of 10 points was applied to the data to smooth it.

3 time greater. This shoulder suggests that there is a minimum in the difference potential very near the center wavelength. This is the case of the Blank potentials. The quantum quasi static approach using the $A^2\Pi_{1/2}$ difference potential predicts a predominately blue shifted line shape. The comparison with the experimental data is shown in Figure 19. The same scaling constant was used for both Figure 17 and Figure 19. This produced a much bigger absorption in the D_1 line. The theory predicts a very sharp peak near the core of the line, this peak is blue shifted in comparison to the actual peak location as the D_2 peak is. In this case the blue peak is about 3 times further out.

The static Anderson-Talman predicted D_1 spectrum (Figure 20) used the $A^2\Pi_{1/2}^+$ difference potential and the same n, s and scaling constant as was used to predict the

47
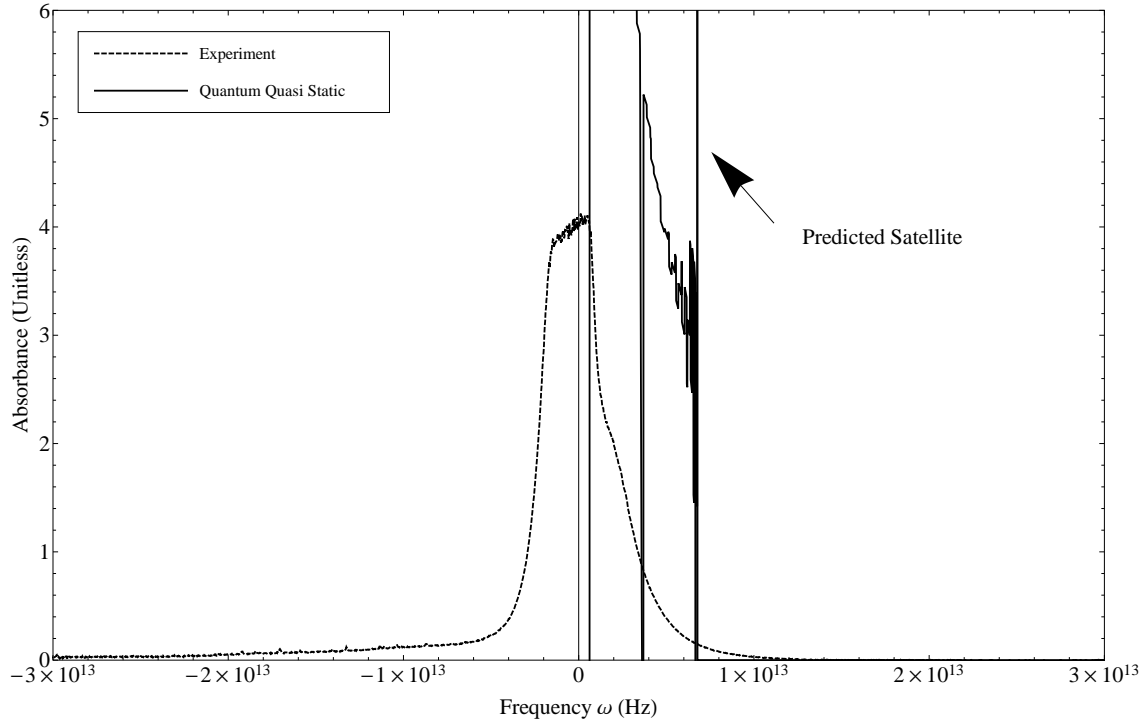
Figure 19. The line-shape and blue shoulder predicted by quantum quasi static theory (Equation 12) compared to measured data for D_1. The measured data was for an Ar pressure of 1124 Torr and $[Cs] \approx 9.4 \times 10^{14}$ cm^{-3}. The scalar constant used to match the predicted line in Figure 17 was also used here.

D_2 line. As expected, the blue shoulder is also shifted to the blue side. The predicted spectrum appears to have a second shoulder that does not appear in the measured spectrum. The predicted magnitude of the entire blue wing is much larger than the measured values so it is possible that if adjustments in scale were made the second shoulder would be to small to be seen by the experiment.

The line-shapes predicted by these static theories produce the right trends and shapes. The potentials can be adjusted to give the right shape, but there may be more than one potential that predicts the right line-shape and particularly for the Anderson-Talman method it is hard to understand how changes in the potentials create changes in the line-shape. As more data is collected for different alkali-noble gas combinations these connections should become more clear.

48

Figure 20. The line-shape and blue shoulder predicted by Anderson-Talman theory compared to measured data for D_1. The measured data was for an Ar pressure of 1124 Torr and $[Cs] \approx 9.4 \times 10^{14}$ cm^{-3}. The constant used to match the predicted line in Figure 18 was also used here. There is a significant amount of ringing from the discreet Fourier transform used to predict the spectrum and some smoothing was applied to the data.

VII. Conclusions

Discoveries

This study presents data of the absorption spectrum of the Cs D_1 and D_2 spectral lines, from 8300 Å to 9100 Å. The primary intent was to observe the spectra at many different pressures and Cs concentrations to determine if there were any significant changes in the line-shape. Figure 16 indicates that there is simply a linear scaling in the line-shape for pressures from 100 torr to at least 1524 torr and Cs concentrations up to $\approx 6 \times 10^{14}$ cm^{-3}. Additionally, it provided experimental data that can be used to help understand the complex relationship between the potential energy surfaces formed between Cs and Ar atoms, and the observed perturbed spectrum. It has been shown that the quantum quasi static theory (Equation 12) can be used to produce the basic structure of the D_2 red wing. Both the quantum quasi static and Anderson-Talman theories predicted the D_2 blue satellite and the D_1 blue shoulder. These were not accurate, but this was expected based on the difference potentials. In each case the difference potentials calculated by Blank [1] were used for the predicted line-shape calculations.

A way of determining the full line-shape of both lines was shown using data collected at several different temperatures. This provides an experimental measure of the difference in height of the satellites and core. The height of the blue satellite with respect to the core calculated by Anderson-Talman was about half of the measured value at 1124 Torr and a Cs concentration of $\approx 6 \times 10^{14}$ cm^{-3}.

Further Study

The proportionality of cross section to Ar concentration was shown to hold up to concentrations of about 3×10^{19} cm^{-3}. At concentrations greater than this, the

50

cross section is no longer proportional in the data collected here. This is likely due to uncertainty in the Cs concentration and path length through the Cs in the heat pipe produced at these high pressures. But, there is the possibility that this is a change in the physics and warrants further investigation [22].

The range of pressures and temperatures that could be examined here was limited by the heat pipe. By utilizing a stronger glass for the windows, the heat pipe could easily hold much higher pressures and more extreme cases could be examined. Also, a slight improvement in the heating block on the pipe would allow higher temperatures to push the limit of alkali concentrations. This would confirm if trends continue such as the linear relationship of line-shape to $[Cs][Ar]L$ in the D_2 blue wing.

The dynamic range of the PMT can be improved by cooling it, allowing a broader and finer determination of $A(\lambda)$. Also, a photo-detector reading the overall intensity of the light coming through the heat pipe would remove many of the uncertainties involved in determining I_0 spectra for a given I collected, such as the effect of the Cs "fog". Along the same lines, if a frequency where absorption was know to take place, such as the blue satellite peak, were monitored over the course of a scan changes in [Cs] concentration over time could be taken into account.

Collecting more line-shapes with different alkalies and perturbing gases would provide more data on how the location of the blue satellite of the D_2 line and the blue shoulder of the D_1 line change with respect to predicted potential energy surfaces. The additional combinations should show a connection between the differences in the potential surfaces, such as those calculated by Blank [1], and the line-shapes. This can provide further insight into how to use the line-shape to find accurate potentials. Ultimately, a better understanding of how DPALs function can be gained, allowing for the best system to be created.

Appendix A.   All Spectra

Absorbance Spectra

The following are plots of all the spectra collected over the course of this research. For a given pressure, the spectra for all measured Cs concentrations are on the same plot. A Log plot of absorbance is given for each.
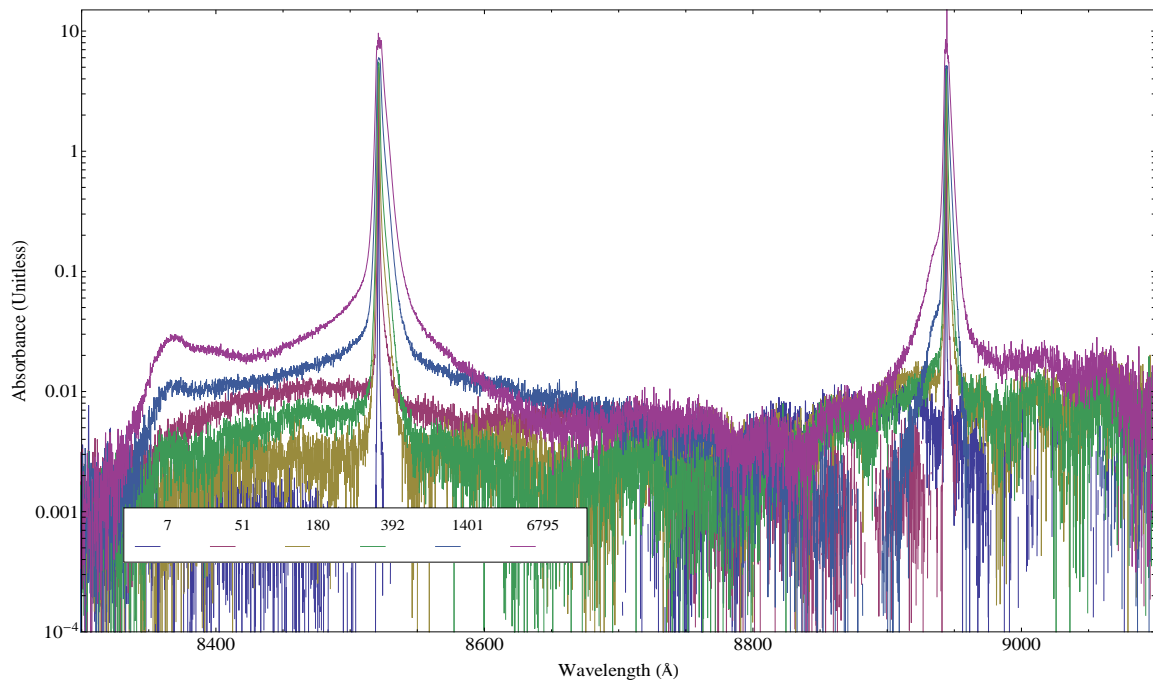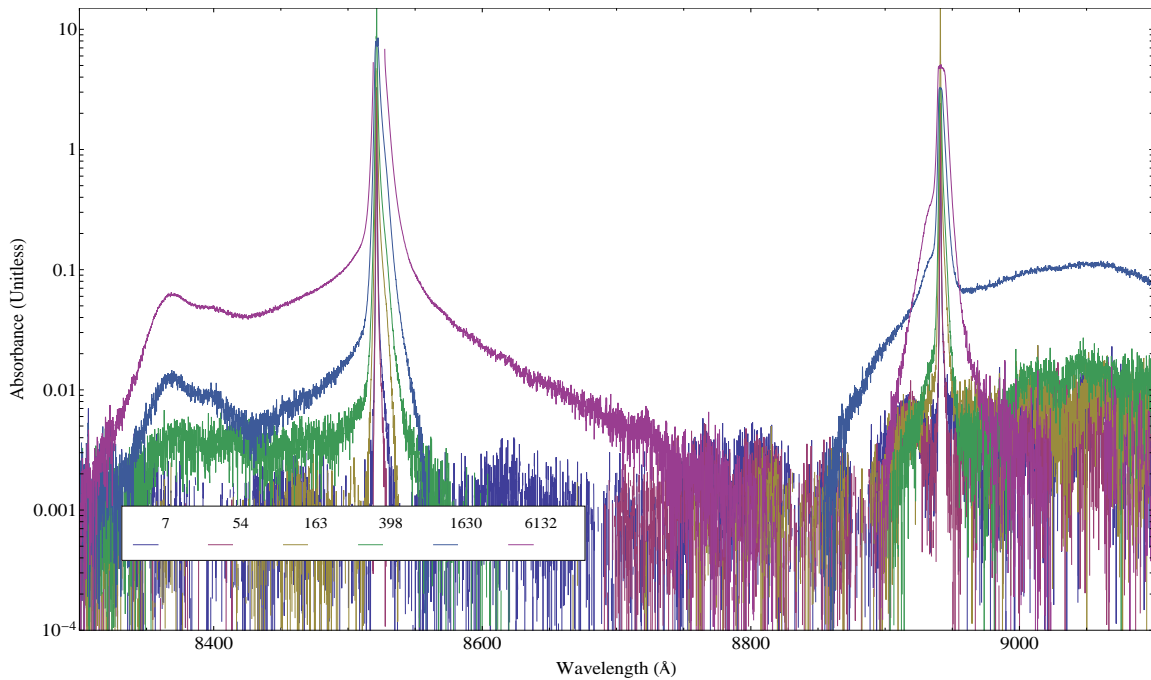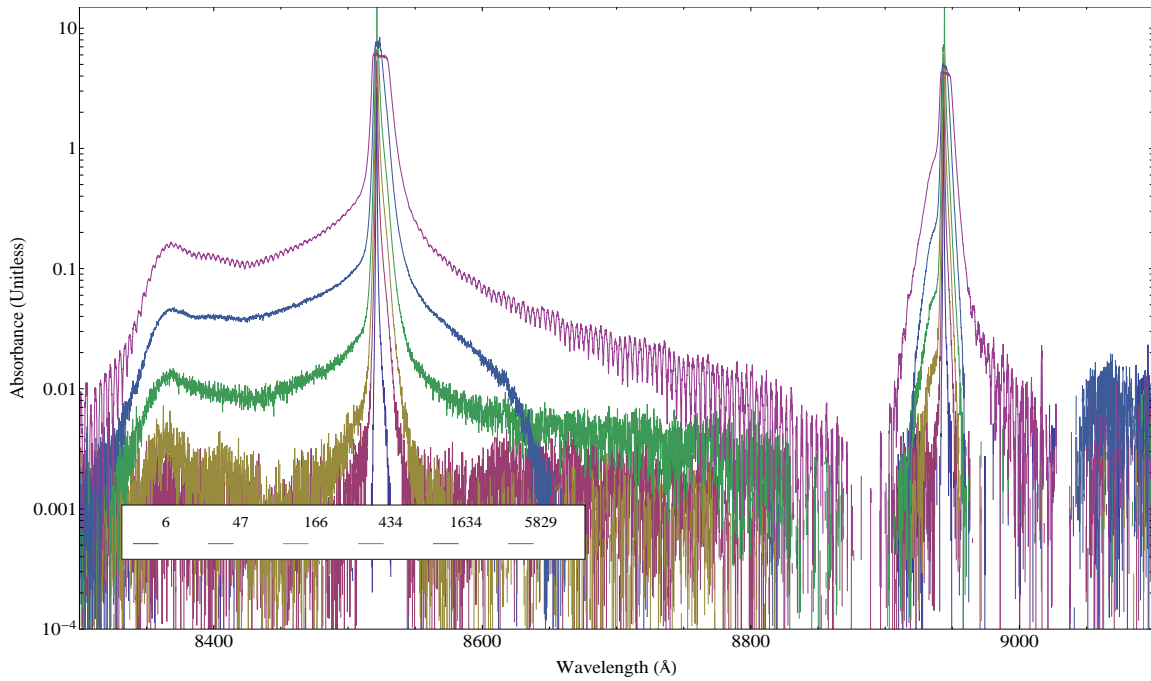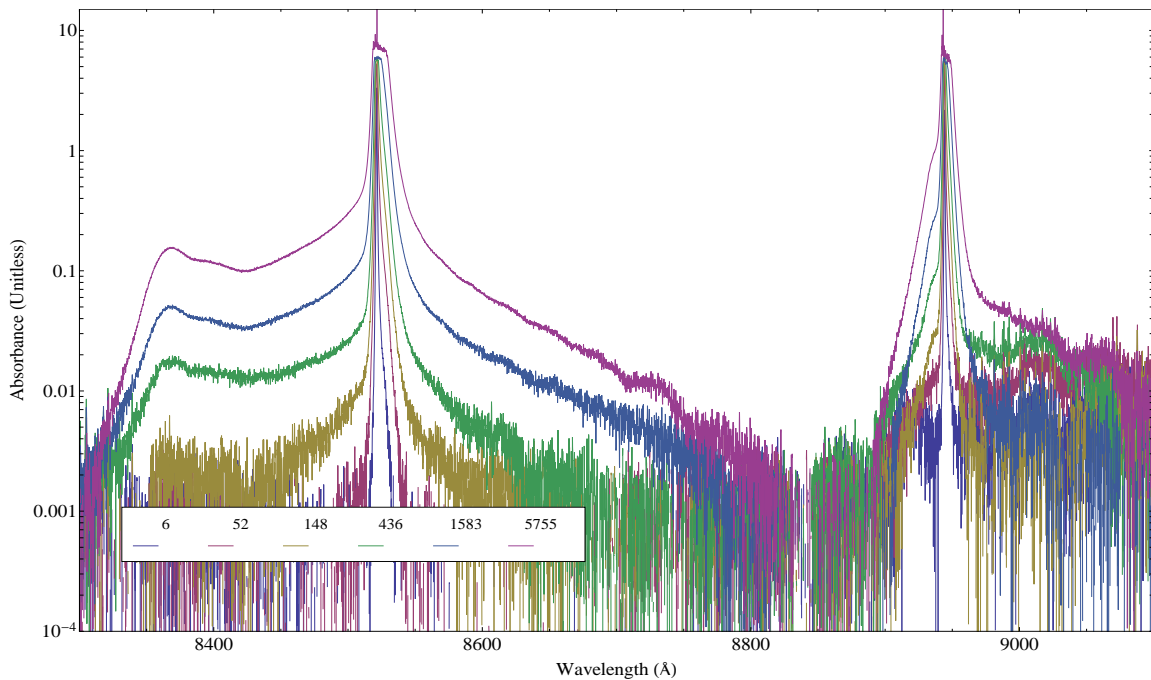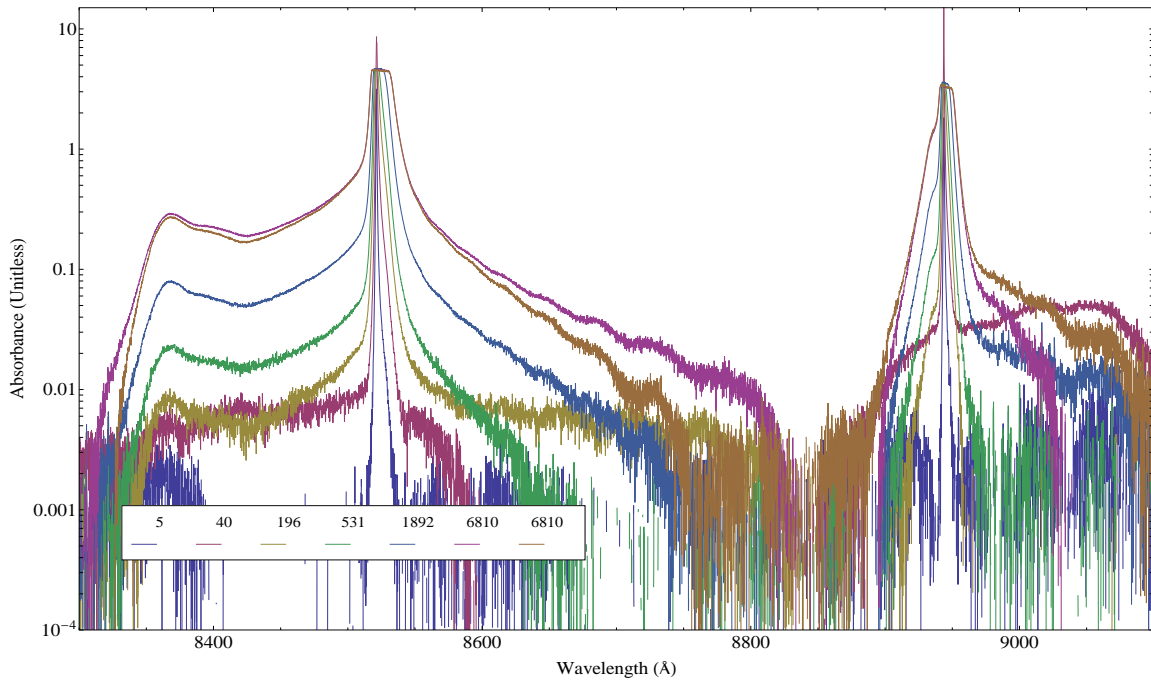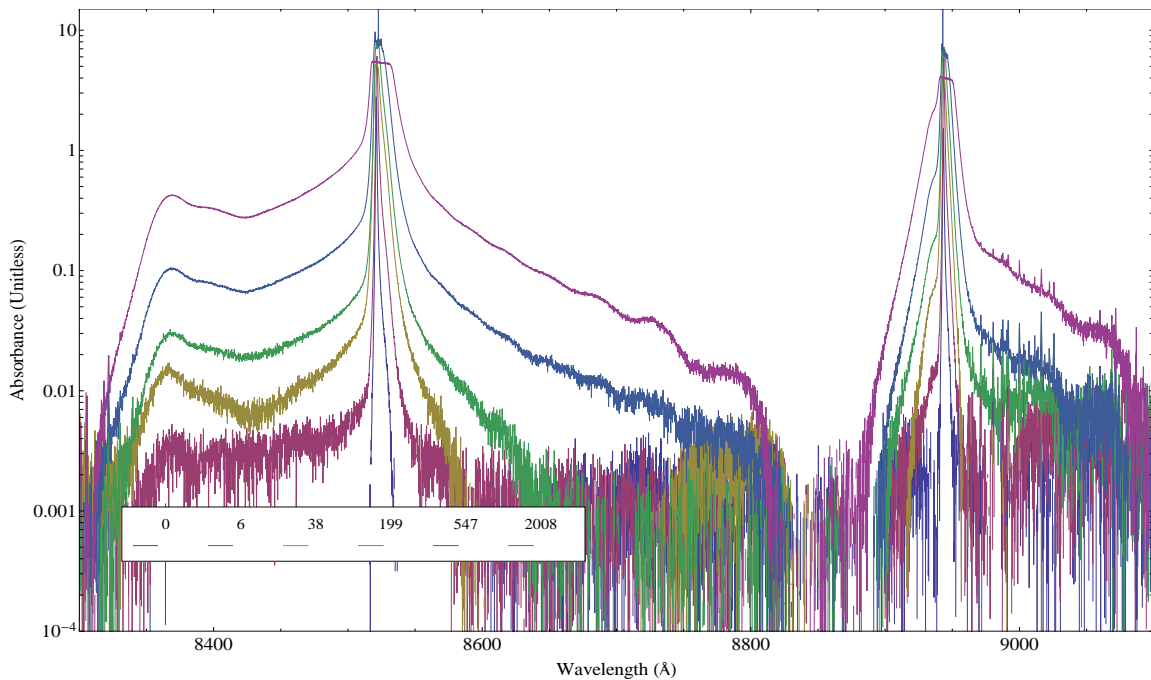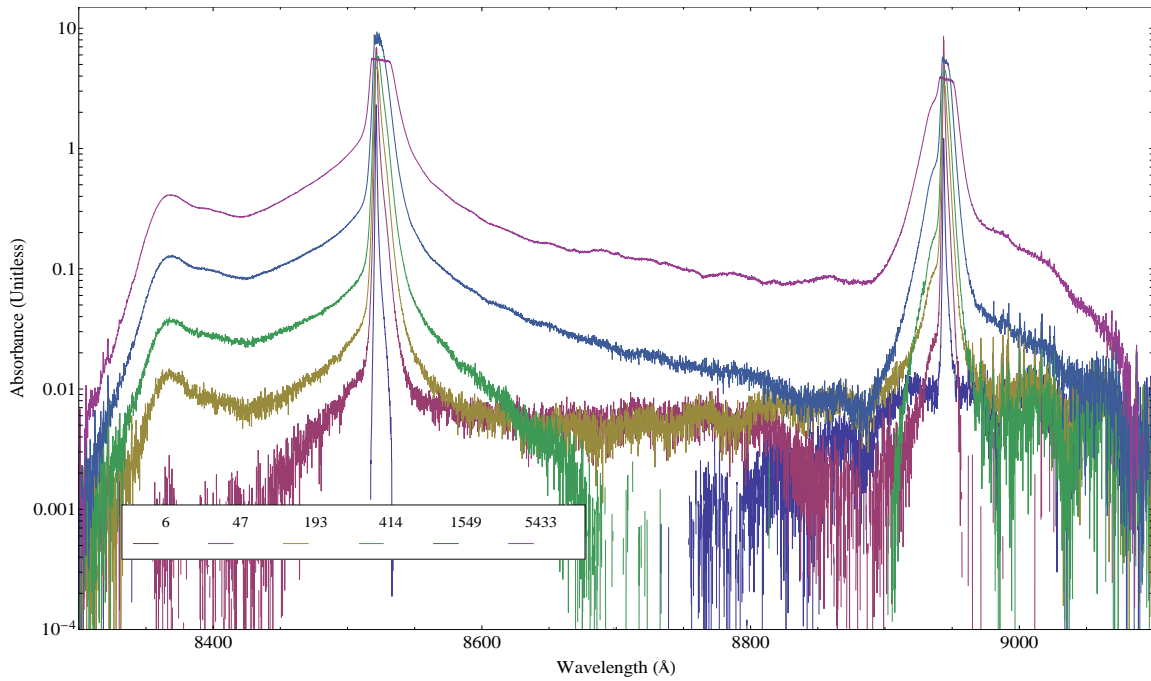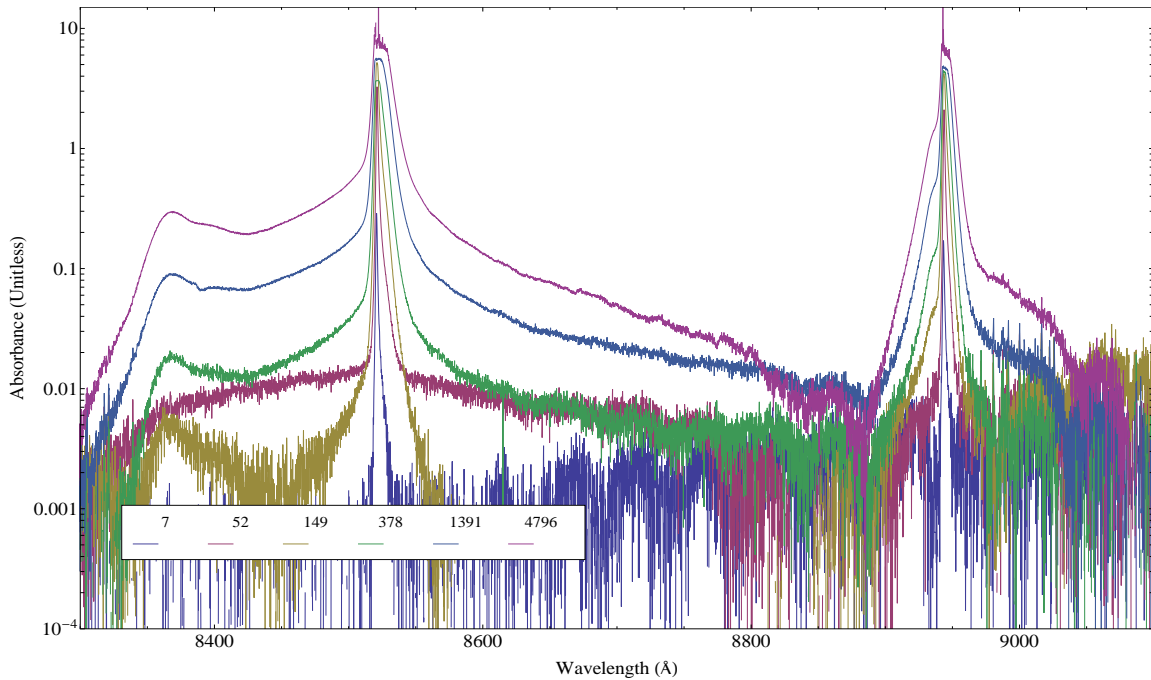

Figure 21. A Log plot of all the spectra collected at 100 Torr of Ar. The units of the legend are 10^{11} cm^{-3}.
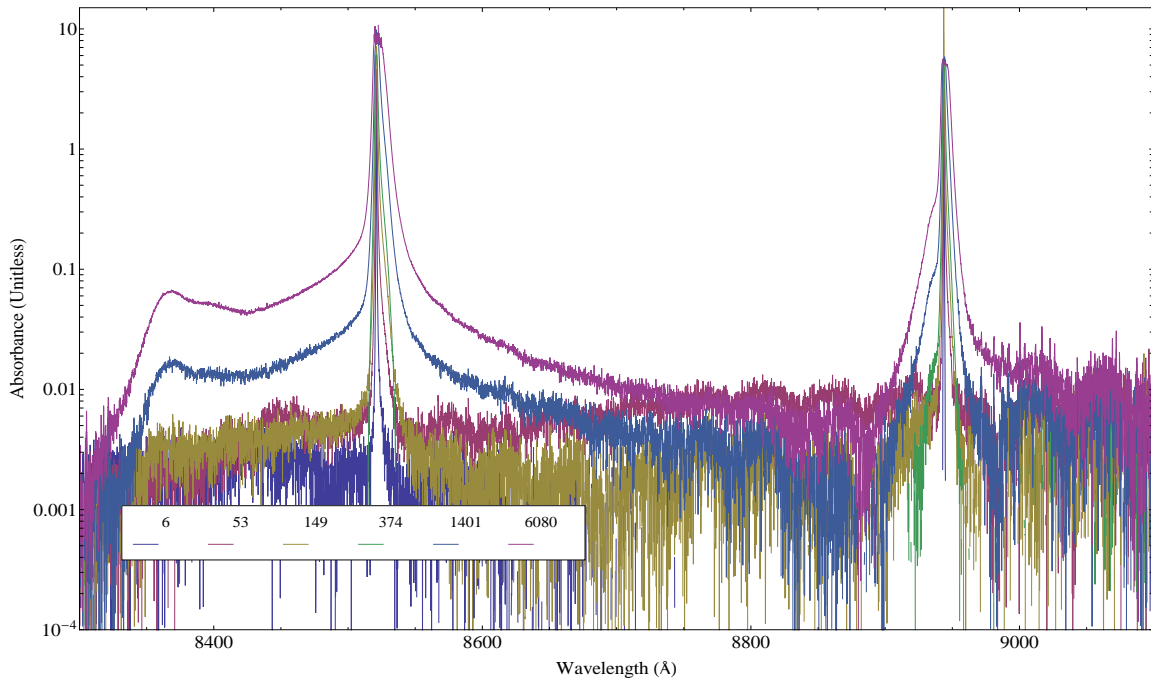
Figure 22. A Log plot of all the spectra collected at 200 Torr of Ar. The units of the legend are 10^{11} cm^{-3}.
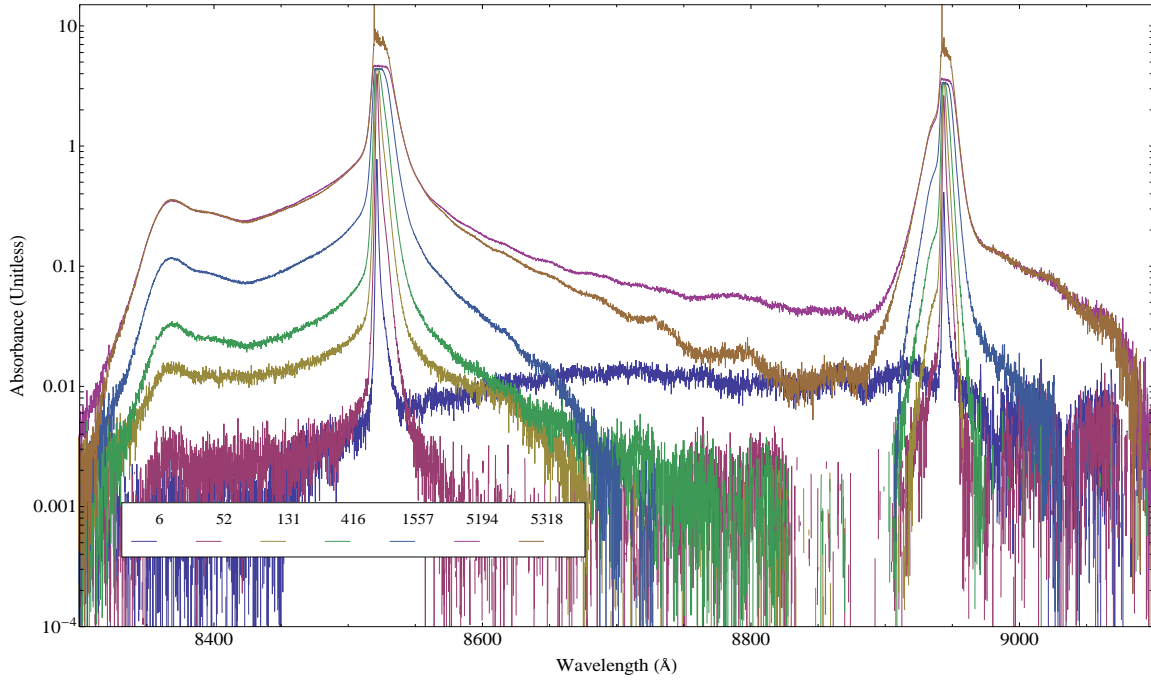

Figure 23. A Log plot of all the spectra collected at 300 Torr of Ar. The units of the legend are 10^{11} cm^{-3}.

Figure 24. A Log plot of all the spectra collected at 400 Torr of Ar. The units of the legend are 10^{11} cm^{-3}.

Figure 25. A Log plot of all the spectra collected at 500 Torr of Ar. The units of the legend are 10^{11} cm^{-3}.

Figure 26. A Log plot of all the spectra collected at 748 Torr of Ar. The units of the legend are 10^{11} cm^{-3}.

Figure 27. A Log plot of all the spectra collected at 1124 Torr of Ar. The units of the legend are 10^{11} cm^{-3}.

Figure 28. A Log plot of all the spectra collected at 1504 Torr of Ar. The units of the legend are 10^{11} cm^{-3}.

Figure 29. A Log plot of all the spectra collected at 1884 Torr of Ar. The units of the legend are 10^{11} cm^{-3}.

56

Figure 30. A Log plot of all the spectra collected at 2280 Torr of Ar. The units of the legend are 10^{11} cm^{-3}.

Cross Section

All the calculated $\sigma(\lambda)$ spectra are presented here. The values are not averaged or in any way smoothed to illustrate how well the data predicted the cross section and the level on uncertainty.

57
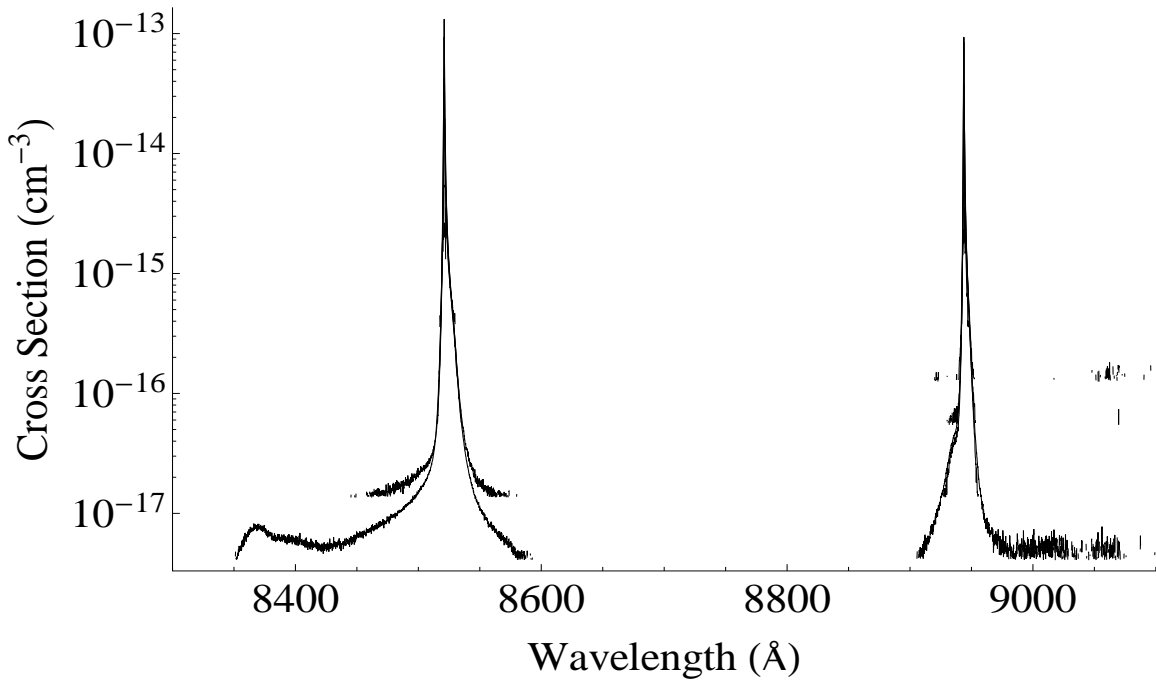
Figure 31. The calculated cross section from each spectrum collected at 100 Torr all plotted together.
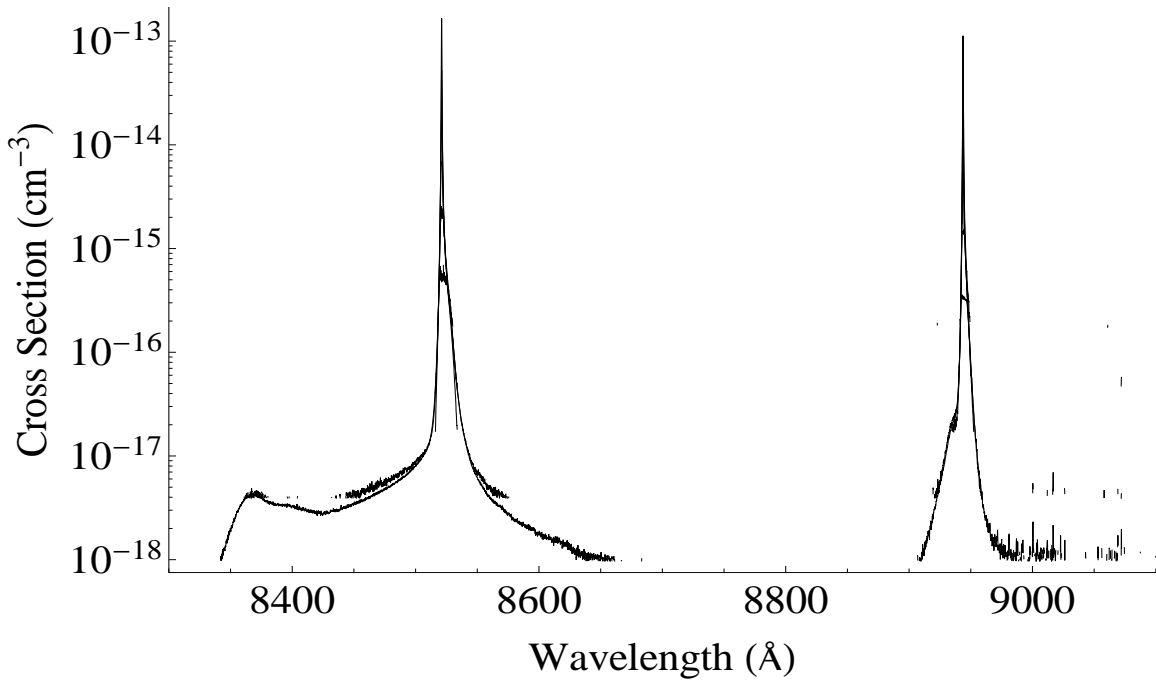
Figure 32. The calculated cross section from each spectrum collected at 200 Torr all plotted together.
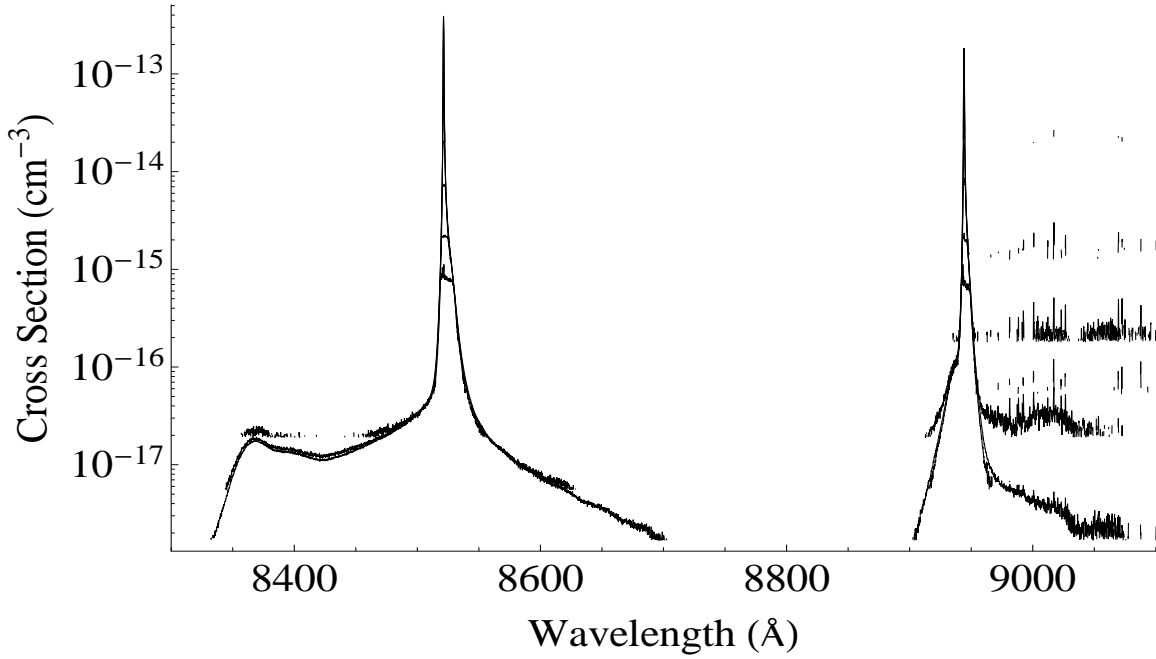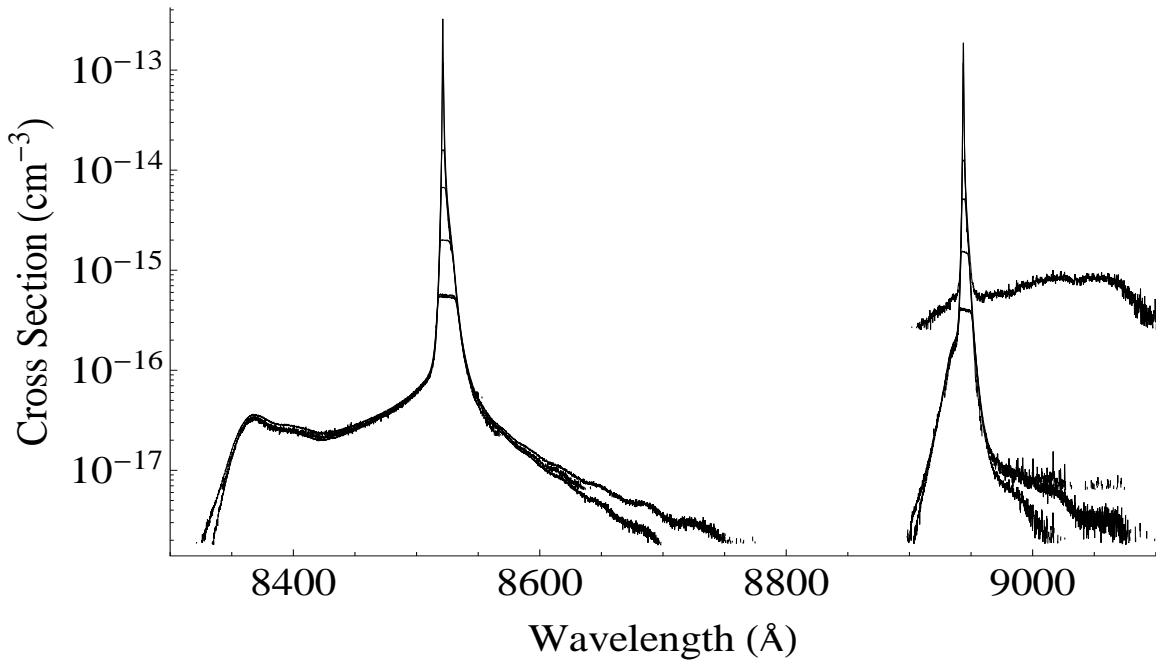
58
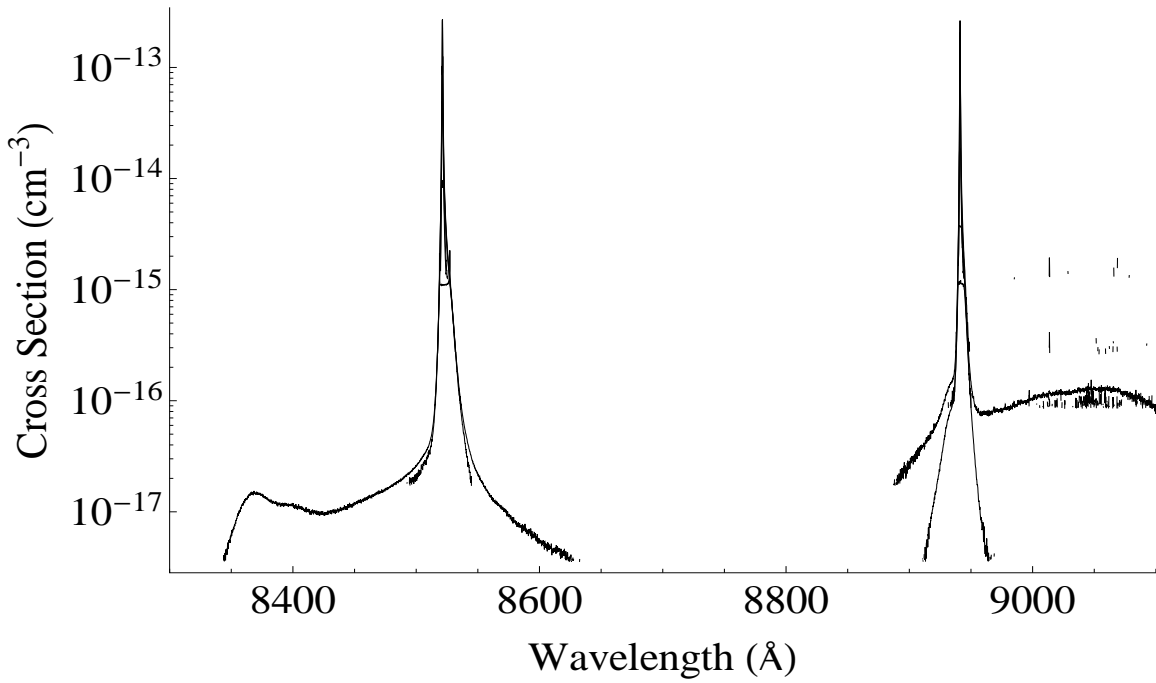
Figure 33. The calculated cross section from each spectrum collected at 300 Torr all plotted together.
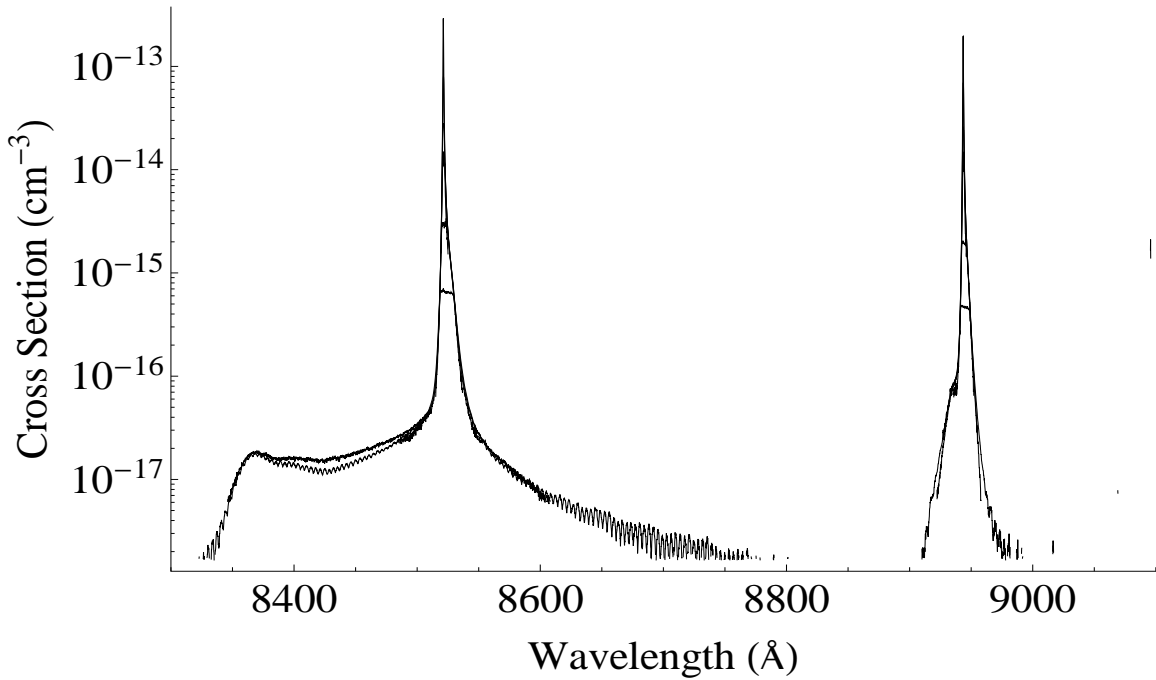
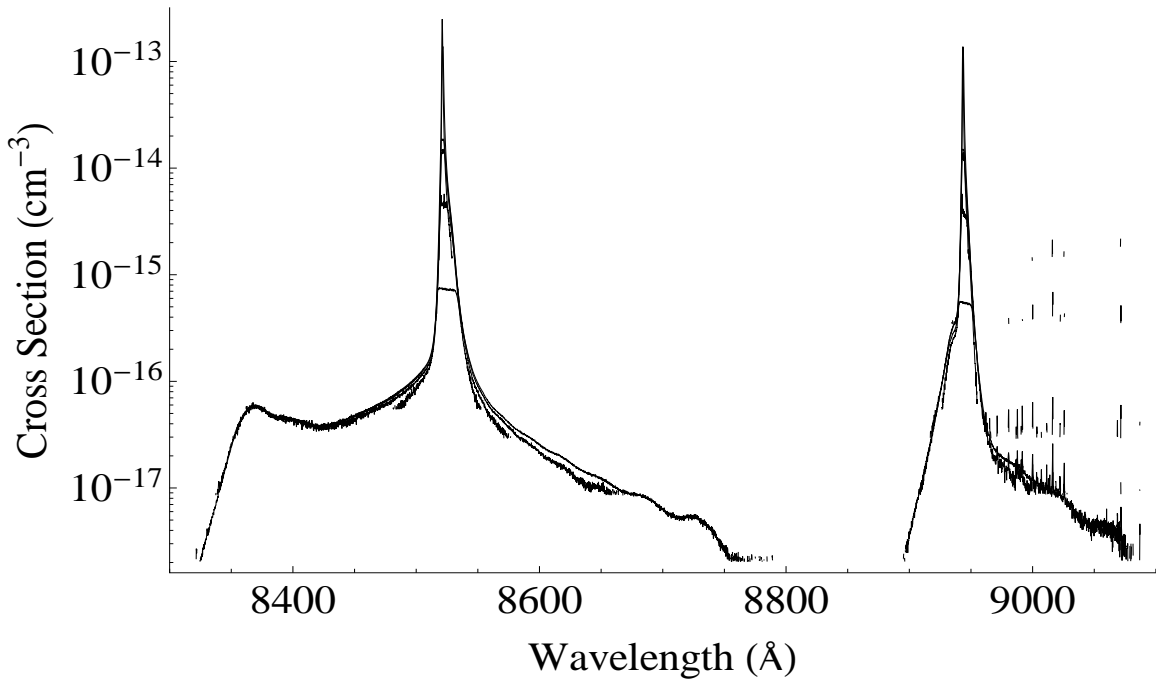**Figure 34.** The calculated cross section from each spectrum collected at 400 Torr all plotted together.

59

Figure 35. The calculated cross section from each spectrum collected at 500 Torr all plotted together.

Figure 36. The calculated cross section from each spectrum collected at 748 Torr all plotted together.

60

Figure 37. The calculated cross section from each spectrum collected at 1124 Torr all plotted together.
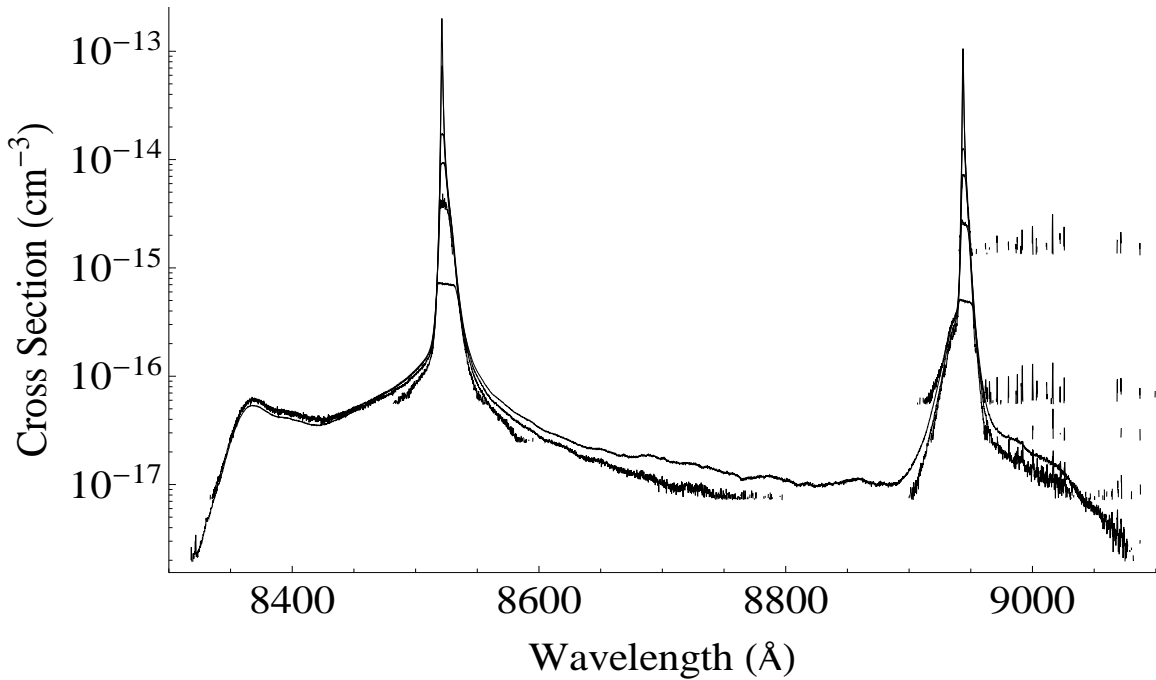

Figure 38. The calculated cross section from each spectrum collected at 1504 Torr all plotted together.
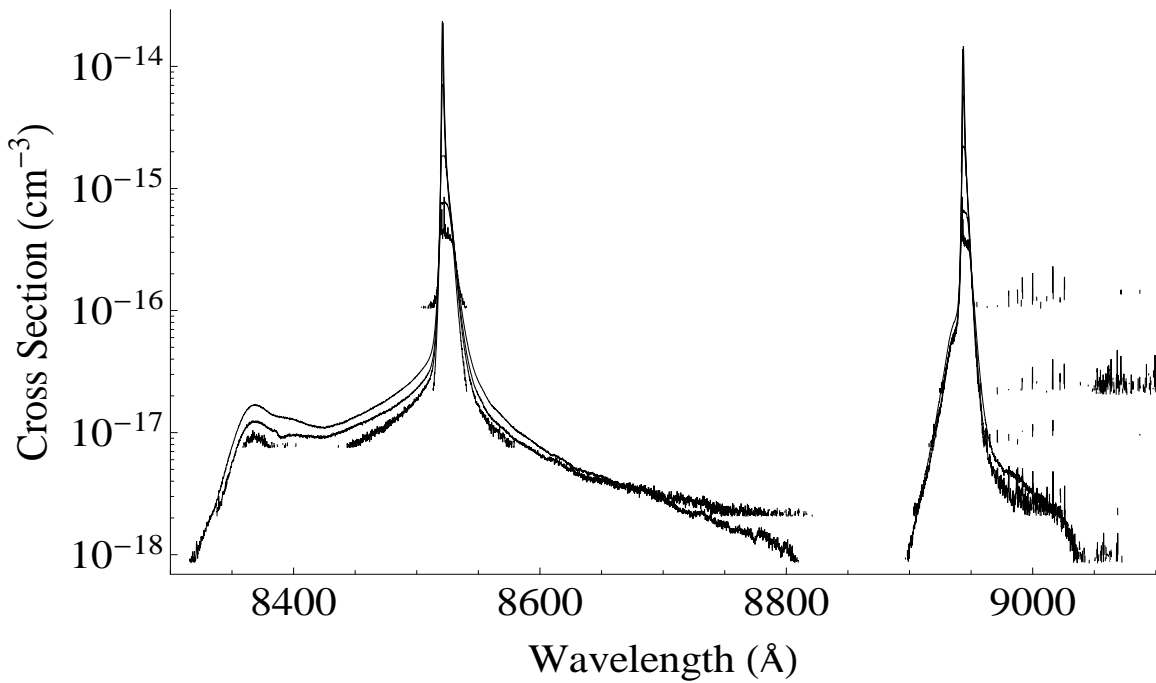
61

Figure 39. The calculated cross section from each spectrum collected at 1884 Torr all plotted together.
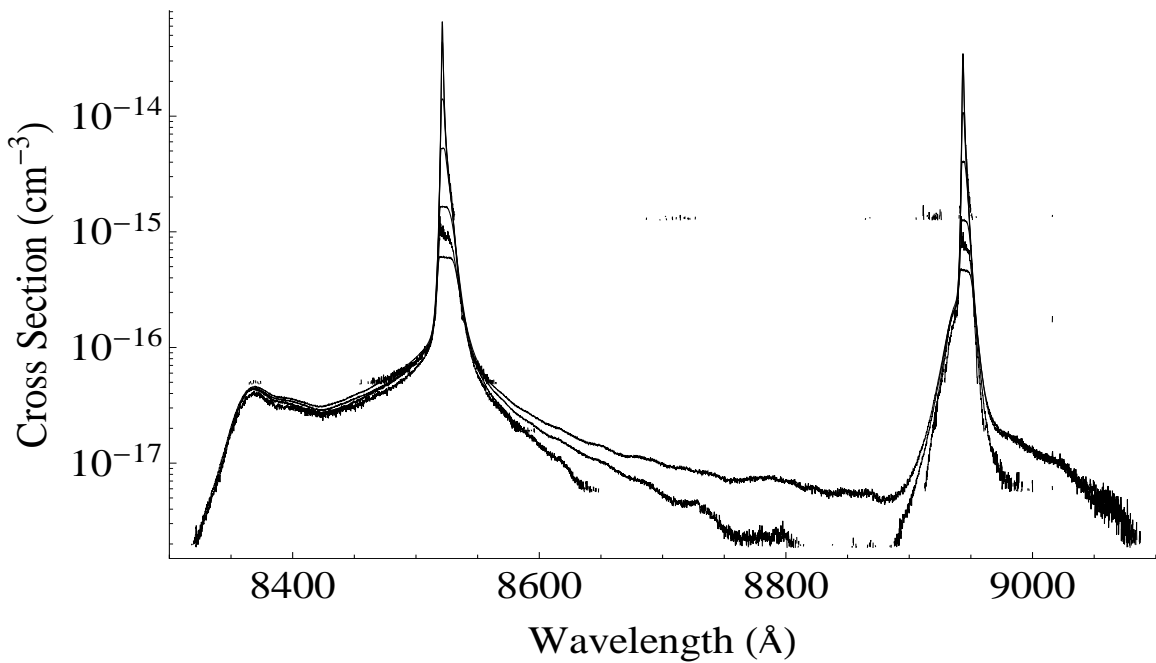

Figure 40. The calculated cross section from each spectrum collected at 2280 Torr all plotted together.

Appendix B. Monochromator Line-shape

The line-shape measured in this series of experiments is a convolution of the instrument line-shape imposed by the monochromator and the actual line-shape of the absorbed light. This convolution can broaden and change the shape of the real spectra trying to be measured. The following gives a description of how the instrument line-shape of this monochromator was investigated.

The instrument line-shape is convolved with each line that is seen in a spectrum and in the case of Cs there are multiple lines at the D_1 and D_2 wavelengths due to the hyperfine structure. The $6^2S_{1/2}$ divides into the hyperfine components $F' = 3$ and $F' = 4$. The $6^2P_{1/2}$ also splits into two levels $F = 3$ and $F = 4$, whereas the $6^2P_{3/2}$ splits into four, $F = 2, 3, 4,$ and 5. By the transition rule $\Delta F = 0, \pm 1$ there are four observed lines in the D_1 line and six in the D_2; the transitions are shown in Table 3.

At zero Torr, taking scans at an increment of 0.025Å, two peaks can be resolved in both the D_1 and D_2 line. Those transitions going to the same $6^2S_{1/2}$ hyperfine level blend together with the instrument-induced line-shape and Doppler broadening. A Voigt defined line-shape, for zero Torr and 50 °C, was calculated for the D_1 and D_2 lines in order to deconvolve it from the measured line and extract the instrument line-shape, Figure 41 shows the Voigt predicted line-shape and the measured line-shape for both lines. *Mathematica* was used to perform the deconvolution. Because the

Table 3. D_1 and D_2 Hyperfine Transitions

Line	Transition $F' \rightarrow F$		Number of Hyperfine Lines
D1	3	3, 4	4
	4	3, 4	
D2	3	2, 3, 4	6
	4	3, 4, 5	

D_2 hyperfine splitting of the $6^2P_{3/2}$ is so small, even the Voigt profile does not show separate lines and the step size of the scan is far too large to see these ($\Delta\lambda \approx .015\mathring{A}$). Because of this, the deconvolution included some of this broadening in the predicted instrument line-shape and it was slightly broader for the D_2 line than what was predicted for the D_1 line. Figure 42 shows the predicted line-shapes.
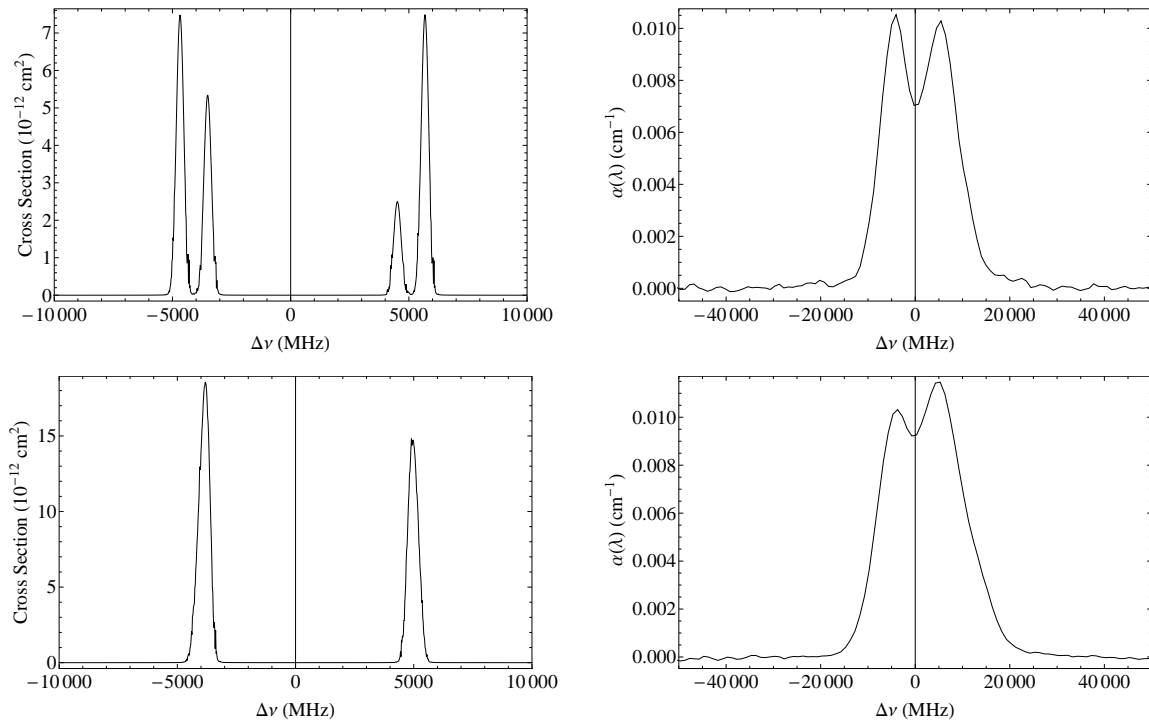

Figure 41. The top row is the D_1 line, the bottom row, D_2. The left column shows the Voigt profile of the cross section at zero Torr and a Cs gas temperature of $50°$C. The right column is the measured line-shapes under the same conditions. The calculation of the Voigt involves numerical integration and at this low a pressure some machine error is introduced which is why the left column plots are jagged.

The FWHM of the instrument line-shapes are comparable to the FWHM of the measured lines when the core is the primary feature (low Cs concentrations). Therefore there is some line broadening due to the instrument line-shape. Once the wings become the primary features, the shape is much broader than the FWHM of the instrument line and hardly effects the shape. The broadening of the core was checked
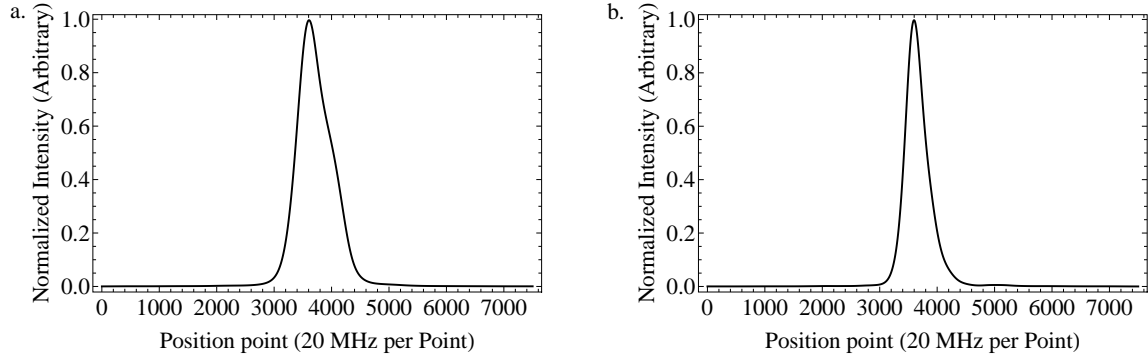
64

Figure 42. The line-shape imposed by the Monochromator determined by deconvolving the theoretical Voigt profile for the core from the measured line-shape, a. is the D_2 line and b. the D_1 line. The step size of the Monochromator was too large to be able to extract all the hyperfine structure from the D_2 line so the instrument line-shape is wider to account for it.

by convolving the predicted instrument line-shape of the D_2 line with a Voigt predicted line at 1125 Torr. The predicted Voigt is shown in Figure 43, and the resulting convolution is compared to the recorded spectrum in Figure 44. The convolution does an excellent job of predicting the line-shape in the core, and the induced broadening is ≈ 6 GHz. The discrepancy in the red wing is caused by non-Lorentzian wing of the line and is not predicted by the Voigt. The instrument line-shape is not introducing any unknown effects and the core line-shape is a Voigt as expected.
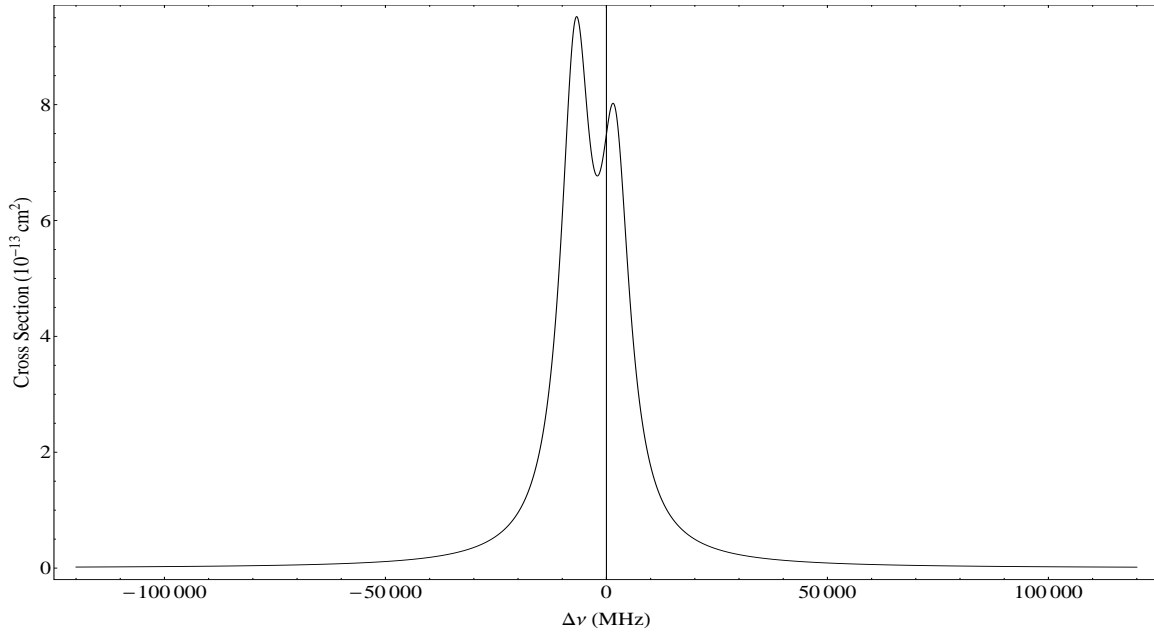
Figure 43. This shows the D_2 cross section predicted for the core at a pressure of 500 Torr and temperature of 50 °C using a Voigt profile.
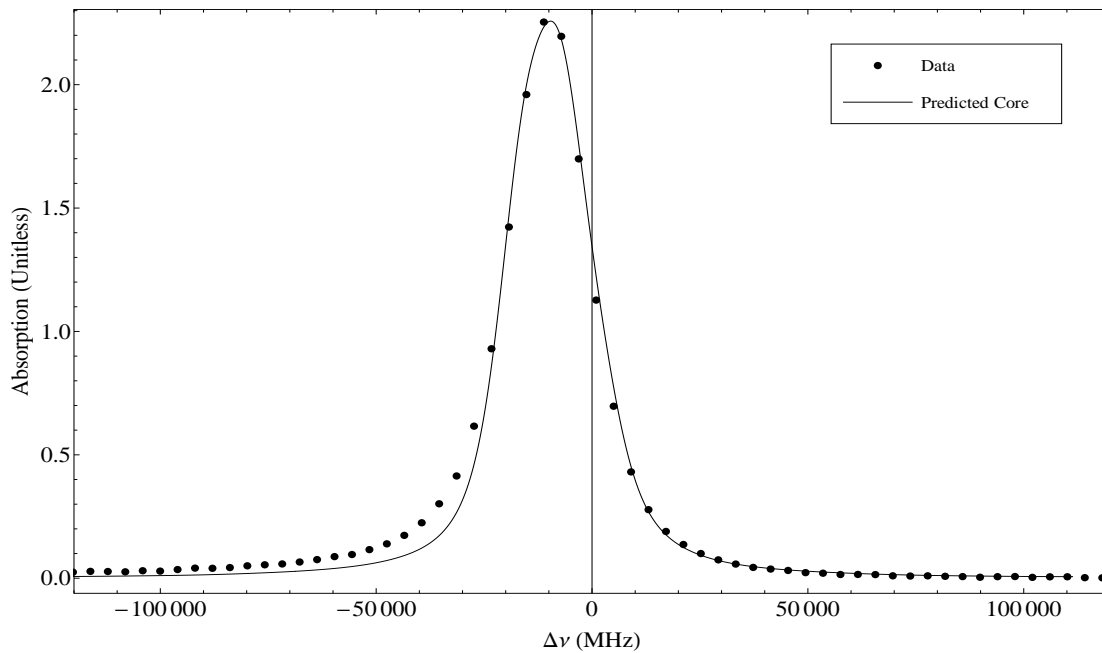

Figure 44. The line shows the line-shape predicted by a 500 Torr broadened Voigt profile for each of the D_2 transition convolved with the extracted instrument line-shape. "Data" is the measured line-shape. The discrepancy on the red side is due to non-Lorentzian effects.

Appendix C. Lamp and Heat Pipe Stability

The overall measured current on the PMT tended to change from scan to scan in what initially seemed a fairly random way. Scans done back to back could be almost on top of each other or as much as 30 nAmps different. Power fluctuations in the lamp power source or the PMT high voltage source were initially thought to be the cause of this. To test this and see if there was a way to remove the effect, the Monochromator was set to a fixed wavelength and data was collected over time. This was done at 8250, 8725 and 9200 Å, for 8.4, 5.2, and 3.1 hours, respectively. The signal did not fluctuate in time very much at all; the standard deviation in current for all three wavelengths for the entire length of the run was $\approx 1.0 \times 10^{-10}$ Amps. This is smaller than the standard deviation on the signal of a standard run over a much shorter time frame, (minutes as opposed to hours). As a result of this data the fluctuations in the PMT gain and source intensity were ruled out.

The general trend of the data is toward lower maximum intensities over time as seen in Figure 45. Transmission through the windows of the heat pipe is likely the cause of this trend, a visible pale substance was seen to grow very slowly, over the course of several weeks, decreasing the transmission through the windows. Other small changes were introduced by the fact that all the focusing lenses and mirror are exposed to the air, allowing for some small random fluctuations in the intensity. The much larger changes are not accounted for in this manor. During one of the scans an oscillation appeared on the signal (Figure 46) that would disappear when the temperature was changed. Inspecting the heat pipe revealed that the Cs was condensing into small macroscopic particles. This had been occurring, unrecognized, for all pressures over 400 Torr at heat pipe temperatures of about 150 °C and higher. These particles scattered visible light and when they formed the overall intensity measured would drop significantly and continue to drop for higher temperatures (Figure 47). These
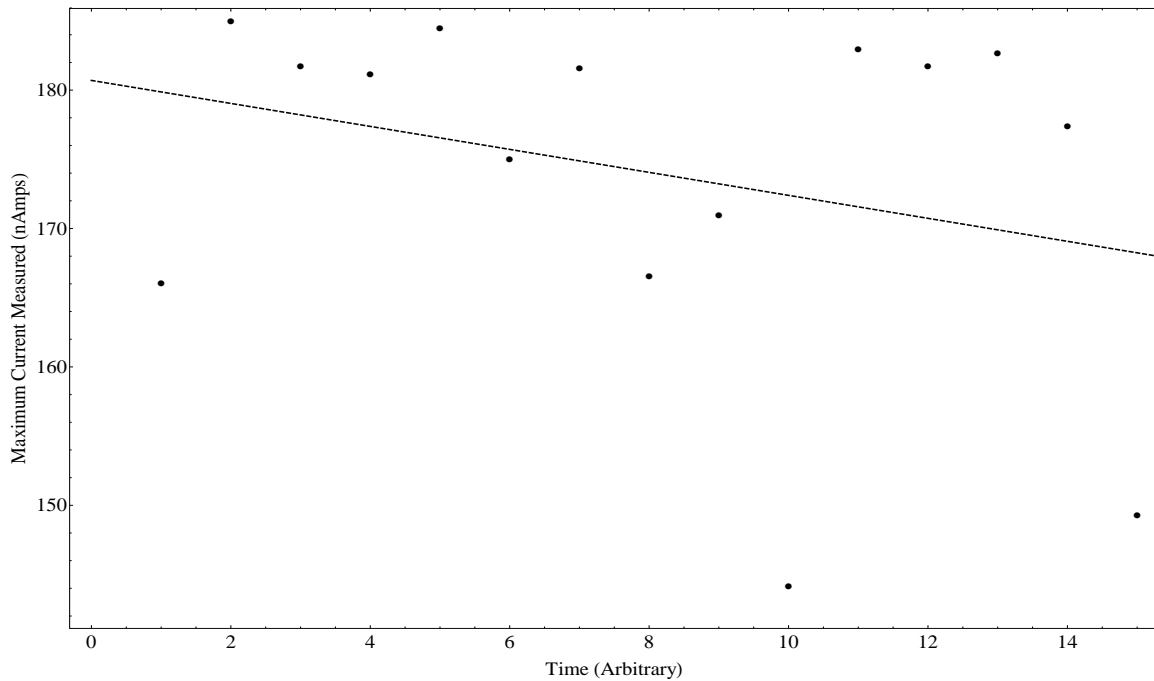
67

Figure 45. The maximum intensity measured on the PMT of each I_0 scan ordered from first to last to show the change over the time of the experiments. There is a general trend downwards as well as an obvious amount of random changes.

two effects satisfactorily explained the changing base line in the spectra collected.

For the course of the experiment, the heat pipe was assumed to be in equilibrium once it had heated to the desired temperature. This was found to not be the case; (Figure 48) shows data collected with the monochromator set to the D_2 line's blue satellite peak (8370Å) with an Ar pressure of 748 Torr and measured over time. There is an initial steep increase in absorption because the heat pipe was initially at room temperature and the pipe was then heated to 150 °C. The absorption then stabilizes for the most part but it continues to slowly decrease over the next 5 hours before appearing to level out. This change in absorption is definitely occurring during a data collection run as they only last 4 hours. This adds uncertainty to $A(\lambda)$, as discussed in Chapter V, and could possibly be removed by recording this data while doing a collection run.
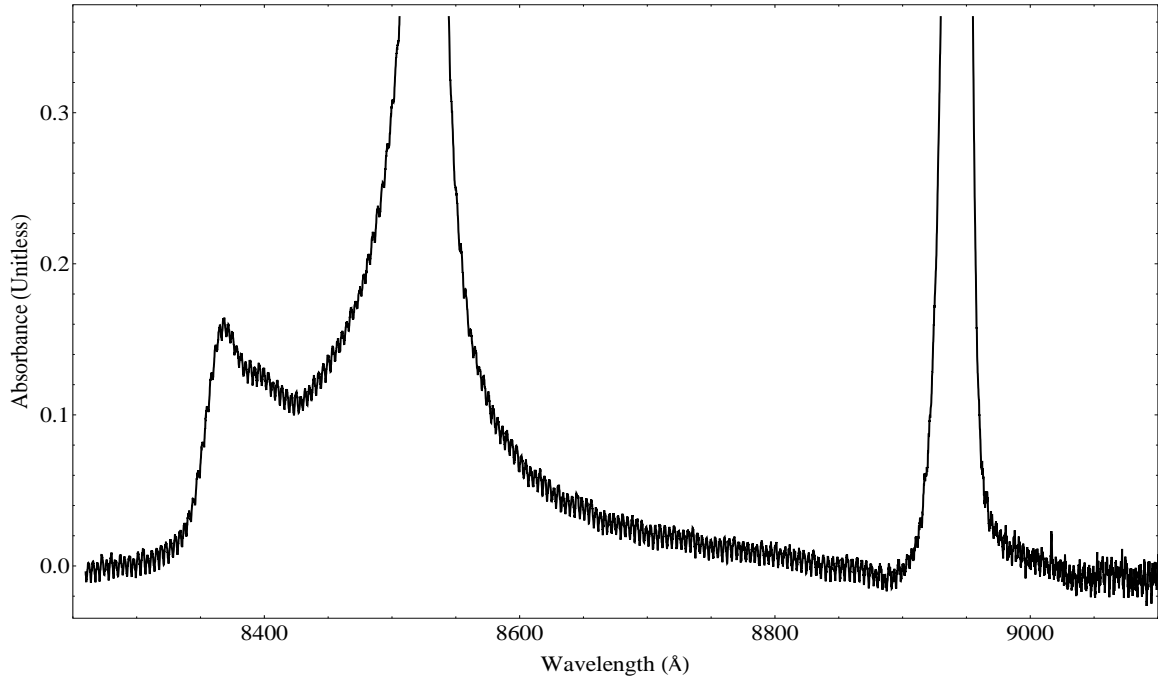
68

Figure 46. This is the spectrum collected that resulted in observing the Cs fog in the heat pipe. The Ar pressure was 400 Torr with $[Cs] \approx 6 \times 10^{14}$ cm^{-3}. The oscillation on the spectrum would disappear at lower heat pipe temperatures as [Cs] decreased.

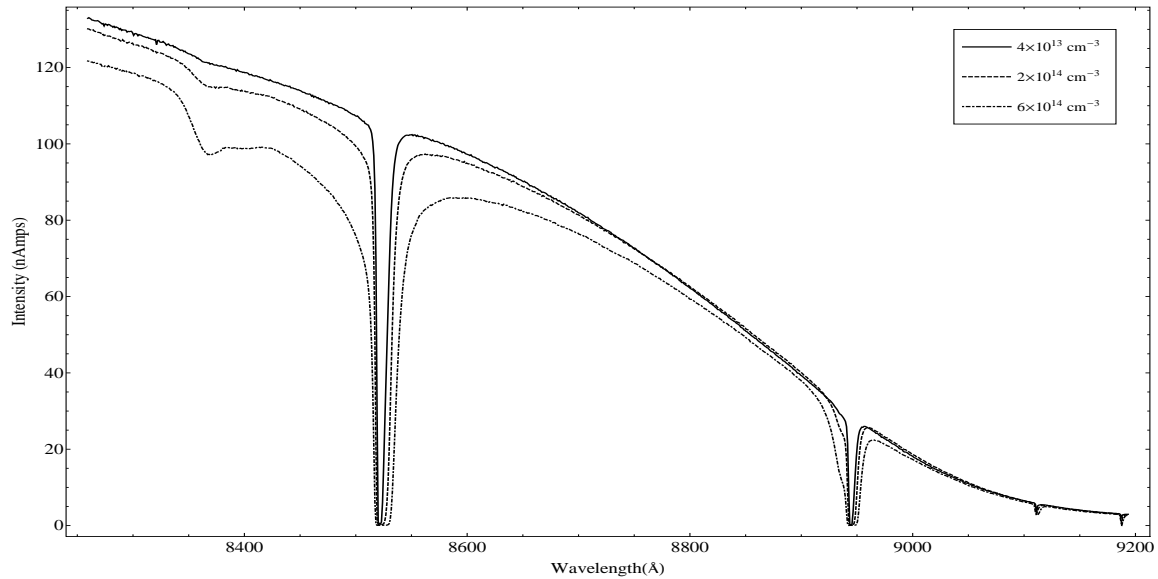**Figure 47.** This shows three successive 500 Torr scans for increasing [Cs], 4×10^{13}, 2×10^{14}, and 6×10^{14} cm^{-3}. As can be seen, the overall intensity drops with each successive [Cs] increase, even outside the absorption region of the spectrum. The Cs fog forming in the heat pipe was dense enough to reduce the overall transmission through the pipe over a broad range of wavelengths.
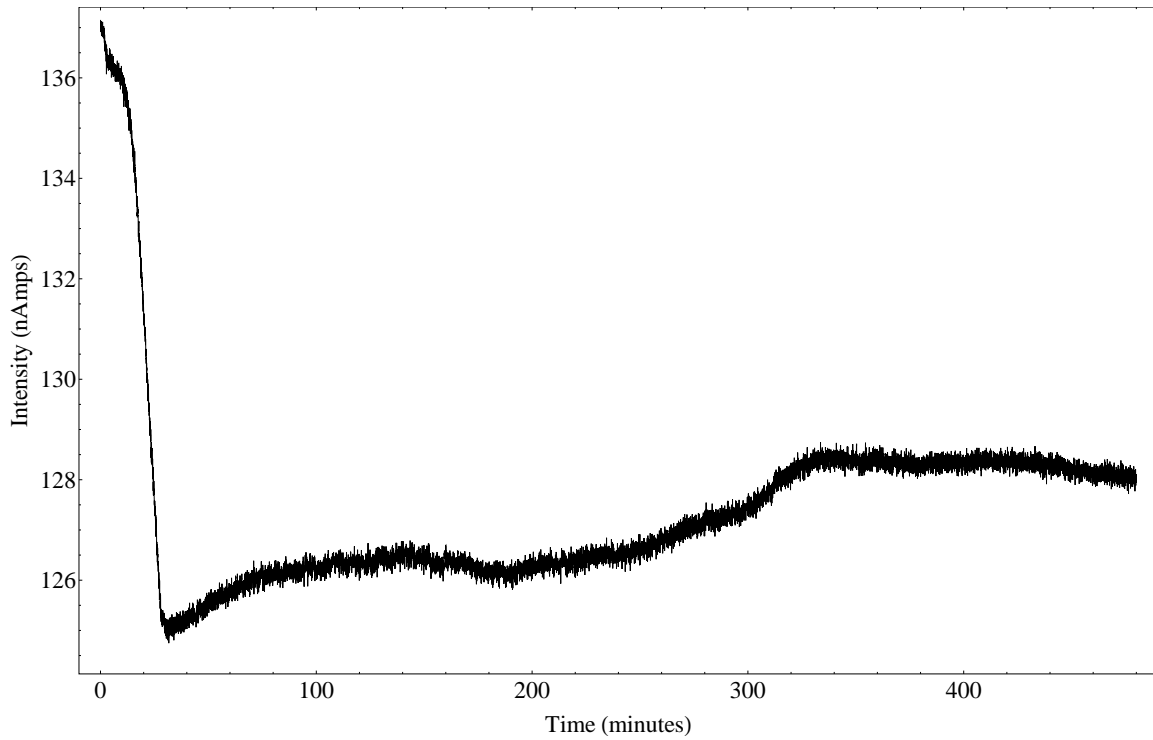
69

Figure 48. This is an approximately 8.5 hour scan with the monochromator set at 8370Å. And shows how the absorption at that wavelength changes with time, indicating the [Cs] in the heat pipe evolves slowly with time. The sharp drop is cause by the heat pipe heating up to 150 °C.

Appendix D. Wavelength Axis Calibration

The spectrum data was recorded with respect to PMT current as a function of stepper motor position. In order to covert the axis to wavelength, two steps were taken. Initially an Oriel krypton pen lamp was used to get a spectrum across a wide range of frequencies. A total of about 13 spectral line were observed (Figure 51). A linear fit relating the motor position to wavelength was found by finding the motor positions of the Kr peaks and associating them with their respective wavelengths according to the Oriel reference lamp wavelength assignments. This fit was used to calibrate the x-axis. But due to slipping of the gears, there were shifts in the peak locations of D_1 and D_2 lines. To accurately calibrate each set of lines, all of the spectra collected at the same pressure were aligned using the D_1 and D_2 line and small atmospheric absorption peaks. The I_0 scans were used to locate the motor position of the D_1 and D_2 lines and these were used to create a linear fit. The fits for each experiment using only the D_1 and D_2 lines and the Kr lamp fit had essentially the same slope, to within ±0.00001 Å per Motor Increment, or ±0.001 Å. Figure 49 shows the HITRAN predicted absorbance for the atmosphere with the measured spectrum's x-axis scaled as described, demonstrating the accuracy of the x-axis calibration. The linearity of the relationship between motor position and wavelength was double checked by looking at the difference of predicted wavelength based on a two point calibration and the actual wavelength of the Kr lines (Figure 50). The difference increases linearly, confirming that there were no non-linear dependency in the conversion from motor position to wavelength.
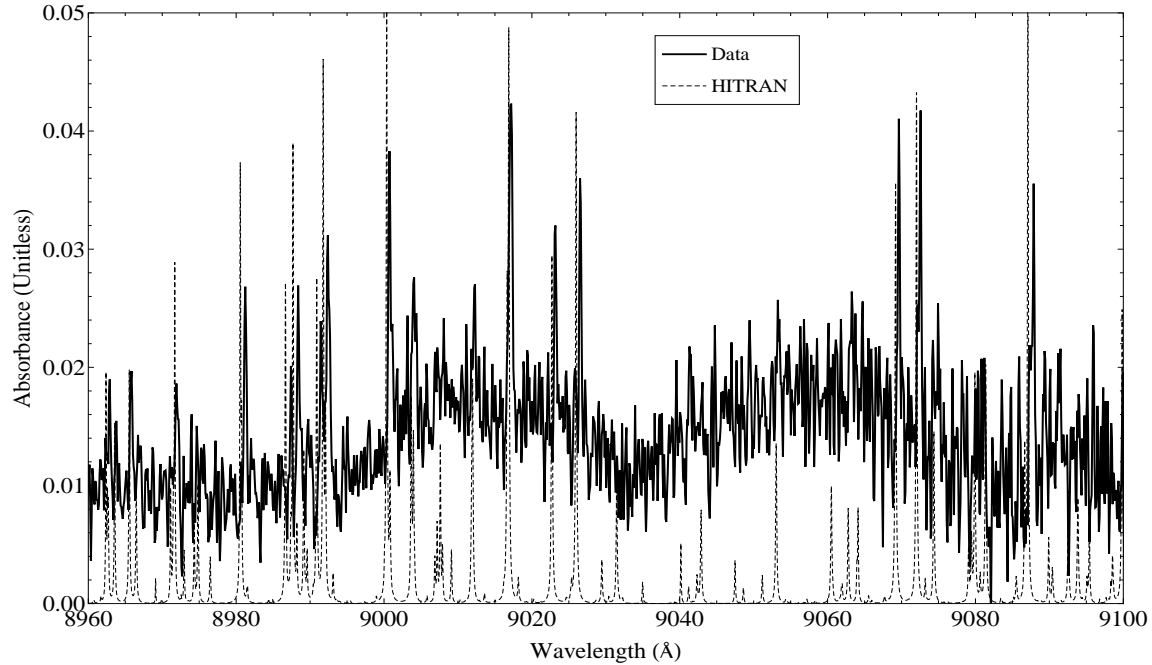
71

Figure 49. The HITRAN predicted spectrum is plotted with a spectrum measured where the atmospheric absorption was strong. The excellent agreement confirmed the accuracy of the wavelength axis calibration.
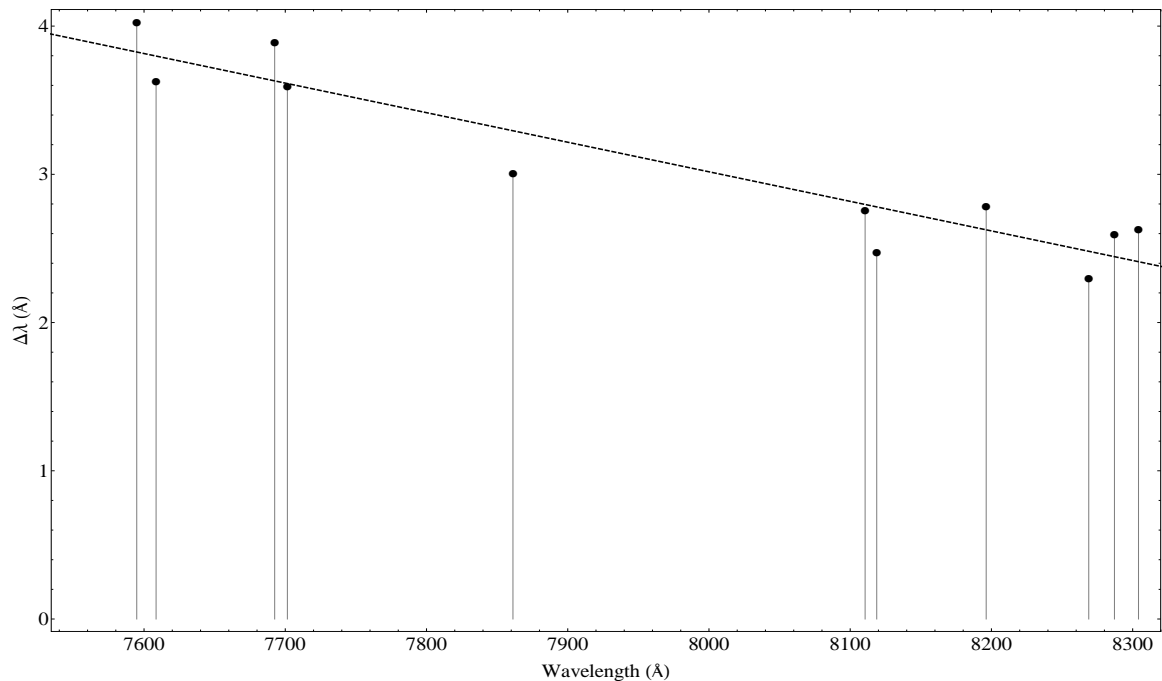

Figure 50. This plots the wavelength calibrated from an I_0 spectrum verses the difference in wavelength between the calculated Kr peak wavelengths and the their actual wavelengths.
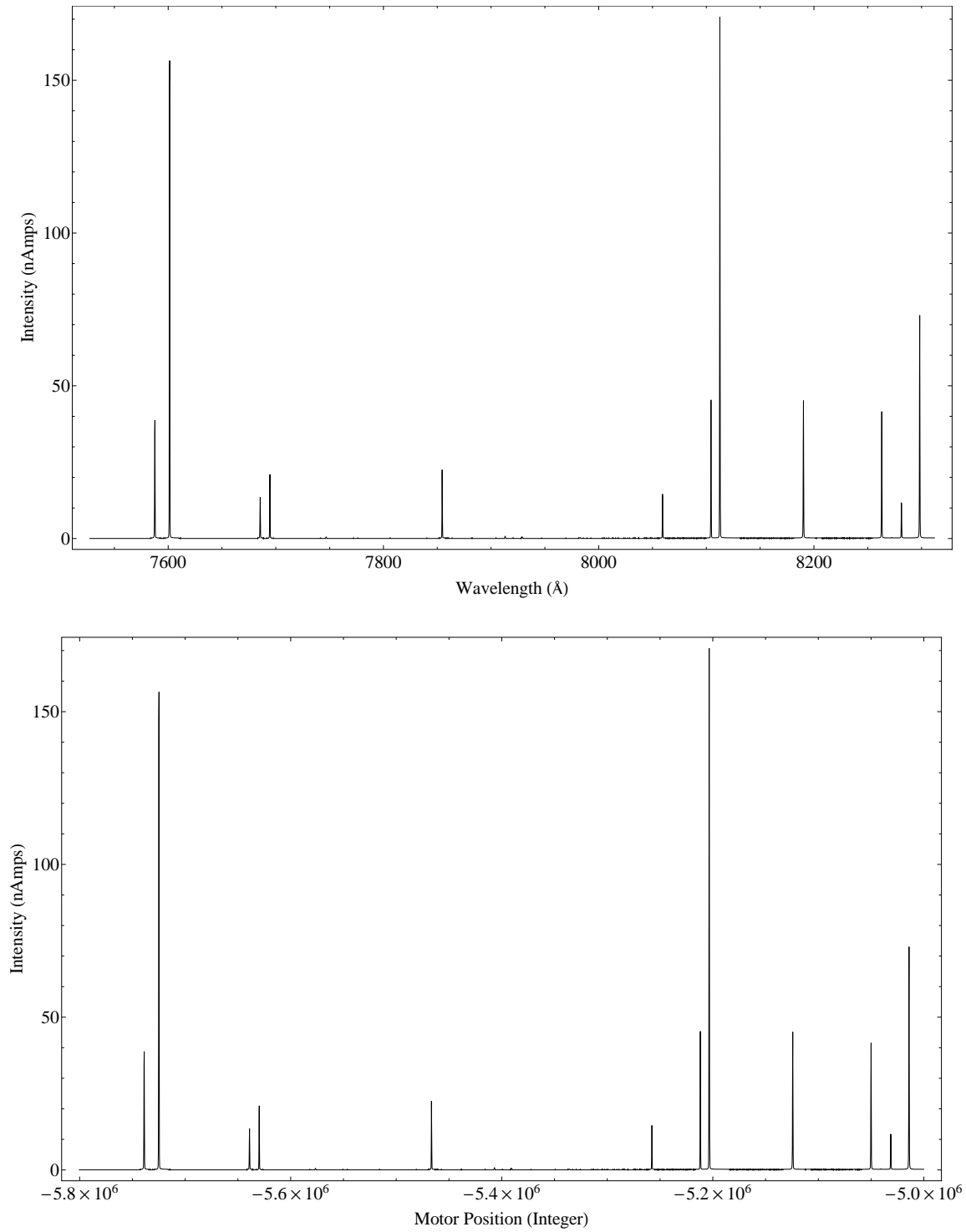
72

Figure 51. These two graphs show the spectrum collected with respect to the recorded motor position (bottom) and the same spectrum with a wavelength calibrated x-axis (top). These are the majority of lines used for the actual calibration.

73

Bibliography

1. L. Blank, Gary S. Kedziora, David E. Weeks. "M+Ng potential energy curves including spin-orbit coupling for M=K, Rb, Cs and Ng=He, Ne, Ar", 2011. Submitted December 2011.

2. Perram, G.P., S.J. Cusumano, R.L. Hengehold, S.T. Fiorino, and Air Force Institute of Technology (US). *An introduction to laser weapon systems.* Directed Energy Professional Society, 2010.

3. Shwartz, J., G.T. Wilson, and J.M. Avidor. "Tactical high-energy laser". *Proceedings of SPIE*, volume 4632, 10. 2002.

4. Hambling, D. "Laser Gunship Fires;'Deniable'Strikes Ahead?" *Wired Blog*, 13, 2008.

5. Krupke, W.F. "Diode pumped alkali lasers (DPALs): an overview". *Proceedings of SPIE*, volume 7005, 700521. 2008.

6. Krupke, W.F. "Diode-pumped alkali laser", November 4 2003. US Patent 6,643,311.

7. Glushko, B.A., M.E. Movsesyan, and T.O. Ovakimyan. "Processes of stimulated electronic Raman scattering and stimulated resonance emission in potassium vapor in the presence of a buffer gas". *Optics and Spectroscopy*, 52:458–459, 1982.

8. Movsesyan, M.E., T.O. Ovakimyan, and S.V. Shmavonyan. "Stimulated processes in a mixture of rubidium vapor and buffer gas under two-photon excitation". *Opt. Spectrosc.(Engl. Transl.);(United States)*, 61(3), 1986.

9. Beach, R.J., W.F. Krupke, V.K. Kanz, S.A. Payne, M.A. Dubinskii, and L.D. Merkle. "End-pumped continuous-wave alkali vapor lasers: experiment, model, and power scaling". *JOSA B*, 21(12):2151–2163, 2004.

10. Gourevitch, A., G. Venus, V. Smirnov, D.A. Hostutler, and L. Glebov. "Continuous wave, 30 W laser-diode bar with 10 GHz linewidth for Rb laser pumping". *Optics letters*, 33(7):702–704, 2008.

11. Pitz, G.A., D.E. Wertepny, and G.P. Perram. "Pressure broadening and shift of the cesium D_1 transition by the noble gases and N_2, H_2, HD, D_2, CH_4, $C_2 H_6$, CF_4, and ^{3}He". *Physical Review A*, 80(6):062718, 2009.

12. Pitz, G.A., C.D. Fox, and G.P. Perram. "Pressure broadening and shift of the cesium D_2 transition by the noble gases and N_2, H_2, HD, D_2, CH_4, $C_2 H_6$, CF_4, and ^{3}He with comparison to the D_1 transition". *Physical Review A*, 82(4):042502, 2010.

13. R., Jason D. *Atomic Alkali Lasers Pumped by the Dissociation of Photoexcited Alkali-Rare Gas Collision Pairs.* Ph.D. thesis, University of Illinois at Urbana-Champaign, 2010.

14. Michelson, A.A. "On the broadening of spectral lines". *The Astrophysical Journal*, 2:251, 1895.

15. Ch'en, S. Y. and M. Takeo. "Broadening and shift of spectral lines due to the presence of foreign gases". *Reviews of modern physics*, 29:20–73, 1957.

16. Allard, N. and J. Kielkopf. "The effect of neutral nonresonant collisions on atomic spectral lines". *Reviews of modern physics*, 54(4):1103, 1982.

17. Szudy, J. and W.E. Baylis. "Profiles of line wings and rainbow satellites associated with optical and radiative collisions". *Physics reports*, 266(3):127–227, 1996.

18. V., Jodeph T. *Laser Electronics.* Prentice Hall, 1981.

19. Fox, C. D. *Radial Distribution of Absorption in a Cesium Heat Pipe with Axial Laser Heating.* Master's thesis, Air Force Institute of Technology, 2011.

20. Fox, C. D. "Lab Notebook". Notebook held personaly, copy availible at Air Force Insitute of Technology.

21. Steck, D.A. "Cesium D line data". *Los Alamos National Laboratory (unpublished)*, 2003.

22. Hedges, R.E.M, D.L. Drummond, and A. Gallagher. "Extreme-wing line broadening and Cs-inert-gas potentials". *Physical Review A*, 6(4):1519, 1972.

REPORT DOCUMENTATION PAGE

1. REPORT DATE (DD-MM-YYYY)	2. REPORT TYPE	3. DATES COVERED (From - To)
22-03-2012	Master's Thesis	May 2011-Mar 2002

4. TITLE AND SUBTITLE

Cesium Absorption Spectrum Perturbed By Argon: Observation of Non-Lorentzian Far Wings

5a. CONTRACT NUMBER

5b. GRANT NUMBER

5c. PROGRAM ELEMENT NUMBER

6. AUTHOR(S)

Lott, Gordon E. 2d Lt USAF

5d. PROJECT NUMBER

5e. TASK NUMBER

5f. WORK UNIT NUMBER

7. PERFORMING ORGANIZATION NAME(S) AND ADDRESS(ES)

Air Force Institute of Technology,
Graduate School of Engineering and Management (AFIT/EN)
2950 Hobson Way,
WPAFB OH 45433-7765

8. PERFORMING ORGANIZATION REPORT NUMBER

AFIT/APPLPHY/ENP/12-M08

9. SPONSORING/MONITORING AGENCY NAME(S) AND ADDRESS(ES)

High Energy Laser Joint Technology Office
801 University Blvd. SE, Suite 209
Albuquerque, NM 87106
Harro Ackermann, (505) 248-8208, harro.ackermann@jto.hpc.mil

10. SPONSOR/MONITOR'S ACRONYM(S)

HEL JTO

11. SPONSOR/MONITOR'S REPORT NUMBER(S)

12. DISTRIBUTION/AVAILABILITY STATEMENT

Distribution Statement A.
Approved For Public Release; Distribution Unlimited.

13. SUPPLEMENTARY NOTES

14. ABSTRACT

The purpose of this research was to observe the core and far wing absorption spectra of the D1 and D2 lines of cesium (Cs) perturbed by argon (Ar). A 1.33 m scanning monochromator with a PMT detector was used to measure the spectra from 8300 Ang. to 9100 Ang.. A heat pipe was used to control the Cs concentration and Ar pressure allowing for a broad range of spectra to be collected. Spectra were collected for heat pipe temperatures of 50, 75, 100, 125, 150 and 175 °C, corresponding to Cs concentrations of approximately 6×10^{11}, 4×10^{12}, 2×10^{13}, 5×10^{13}, 2×10^{14}, and 9×10^{14} cm^-3. This was done for each Ar buffer gas pressure of 100, 200, 300, 400, 484, 746, 1124, 1504, 1884, and 2280 Torr. The D2 blue satellite absorption line was measured at a wavelength of 8367 ± 0.8 Ang. for Ar pressures from 500 to 2280 Torr. A linear relationship between the D2 wing cross section and increasing Ar pressure was observed for pressures from 100 to 1504 Torr. Measured spectra were compared to spectra produced by two theoretical models the quantum quasi static approach and the static limit of Anderson-Talman theory.

15. SUBJECT TERMS

Non-Lorentzian Line-Shapes, Cesium Absorption Spectrum, DPAL, Pressure Broadening, XPAL, Cesium D2 Blue Satellite, Alkali Laser

16. SECURITY CLASSIFICATION OF:			17. LIMITATION OF ABSTRACT	18. NUMBER OF PAGES	19a. NAME OF RESPONSIBLE PERSON
a. REPORT	b. ABSTRACT	c. THIS PAGE	SAR	88	Glen Perram AFIT/ENP
U	U	U			19b. TELEPHONE NUMBER (Include area code) 785-3636 x4504; glen.perram@afit.edu

Reset